Geochronology and geochemistry of Meso- to Neoarchean magmatic epidote-bearing potassic granites, western Dharwar Craton (Bellur–Nagamangala–Pandavpura corridor), southern India: implications for the successive stages of crustal reworking and cratonization

M. Jayananda, Martin Guitreau, T. Tarun Thomas, Hervé Martin, K. Aadhiseshan, R. Gireesh, Jean-Jacques Peucat, M. Satyanarayanan

Geochronology and geochemistry of Meso- to Neoarchean magmatic epidote-bearing potassic granites, Western Dharwar Craton (Bellur-Nagamangala-Pandavpura corridor), Southern India: Implications for the successive stages of crustal reworking and cratonization

M.Jayananda[1*], Martin Guitreau[2], T. Tarun Thomas[1], Hervé Martin[2], K.R. Aadhiseshan[3], R.V.Gireesh[3]., Jean-Jacques Peucat[4] and M. Satyanarayanan[5]

[1] Centre for Earth, Ocean and Atmospheric Sciences, University of Hyderabad, Gachibowli, Hyderabad – 500 046, India

[2] Université Clermont Auvergne, Laboratoire Magmas et Volcans, IRD, CNRS, UMR 6524, 6 Avenue Blaise Pascal, 63178 Aubière, France.

[3]Department of Geology, University of Delhi, Delhi-110 007, India

[4]Geosciences Rennes, Université Rennes I, Rennes, 35042 France.

[5]CSIR-National Geophysical Research Institute, Uppal Road, Hyderabad – 500 007, India

*Corresponding author (e-mail : mjayan.geol@gmail.com)

Keywords: Zircon U-Pb geochronology, Dharwar craton, Archean, potassic granite, magmatic epidote, cratonization.

Abstract:

The present study addresses successive stages of Meso-to Neoarchean crustal reworking, potassic granite magmatism, and craton forming processes in a crustal corridor between the Western and Central Dharwar craton (Southern India). We present field, petrographic characteristics, zircon U-Pb ages, Nd isotopes, major and trace element data for the granitic plutons from this corridor. Field relationships reveal three stages of plutonism including: (1) sparse plutons intruding the TTG basement away from the western boundary of the

Nagamangala greenstone belt (2) plutons adjoining the Nagamangala greenstone belt and (3) plutons to the south of Nagamangala greenstone belt in the Pandavpura region. Petrographic characteristics of plutons within TTG basement reveal dominantly granodioritic composition whilst plutons found at the contact with Nagamangala greenstone belt are dominantly monzogranitic, quartz-monzoniti and granodioritic in composition. On the other hand, plutons in Pandavpura region have monzogranite to quartz-monzonite composition. Zircon U-Pb ages show that the plutons emplaced in three distinct periods, wherein plutons in TTG basement emplaced at ca. 3.2 Ga, whilst plutons adjoining greenstone belt show ages of ca. 3.0 Ga, and plutons in the Pandavpura region yield ages ca. 2.6 Ga. Major and trace element data of the 3.2 Ga granodiorite indicate their origin through melting of mafic protoliths without any significant residual garnet. REE have poorly fractionated patterns with negative Eu anomalies together with Nd model ages of ca. 3.0 Ga. These plutons show that crust played a prominent role in their genesis while mantle component remained subordinated. Melts derived from those two components interacted through mixing and mingling as evidenced by field relationships, Harker binary diagrams and Nd isotope data. REE have poorly fractionated patterns with negative Eu oanomalies. All these evidences indicate that these ca. 2.6 Ga plutons resulted of crustal melting leaving aplagioclase-bearing residue. The presence of magmatic epidote in all the studied granites points to their crystallization at pressure of at least 5 kbars (~15km depth). The 3.2 Ga intrusions could correspond to the reworking associated with the terminal event of a major juvenile crust forming episode whilst 3.0 Ga potassic granites corresponds to cratonization of the WDC throughout which melting of the deep crust resulted in depletion of heat producing elements, eventually, leading to an efficient cooling of the deep continental crust. The ca. 2.6 Ga Pandavpura granite could represent final stabilization of the WDC as the 2.5 Ga granite magmatism is absent.

1. Introduction

Study of continental evolution and craton forming processes have been major themes of research in Earth Sciences over the last three decades (e.g., Cawood et al., 2013). Understanding the origin of protocontinents is important as it is linked with chemical and thermal evolution of the Earth mantle as well as emergence of life. The major uncertainty regarding Archean protocontinent formation is that most models propose extensive juvenile crust accretion (e.g., Taylor and McLennan, 1985; Roberts and Spencer, 2014). However, present-day crust distribution is apparently inconsistent with such hypothesis (Goodwin, 1996) and would indicate important crust recycling into the mantle and/or crustal reworking leading to generation of potassic granitoids. Most models proposed for the Archean crustal evolution are based on the balance between new juvenile crust additions and reworking of pre-existing continental crust (e.g, Allègre and Rousseau, 1984; Iizuka et al., 2005; Kamber, 2015). Major and trace elements, as well as radiogenic and stable isotope data, show that juvenile accretion was the dominant process during the Eoarchean to the Paleoarchean that contributed to Archean continental growth whilst reworking processes became progressively more important from Neoarchean onwards (e.g., Valley et al., 2005; Kamber, 2015; Jayananda et al., 2006, 2018). This pattern is also visible within the evolution of Archean cratons which show juvenile addition of material (TTG suites; e.g., Moyen and Martin, 2012) until it undergoes reworking that leads to the formation of potassic granites (e.g., Martin et al., 1997; Laurent *et al.*, 2014;Moyen et al., 2003). These reworking events are spatially linked to major thermal event and stabilization of Archean continental crust (e.g. Jayananda et al., 2006; Laurent *et al.*, 2013, 2014). However, the details of the petrogenetic reworking mechanisms, their link to juvenile accretion, thermal events and cratonization of Archean crust are still under debate.

The Archean Dharwar craton (e.g., Jayananda et al., 2018) is an ideal target (Fig.1) to address the issue of relative inputs of juvenile additions and crustal reworking in Archean

77 crustal evolution as well as spatial link between juvenile accretion, tectonothermal events,
78 crustal reworking and cratonization. Several potassic granite plutons are exposed close to the
79 eastern margin of the Western Dharwar Craton (WDC) in an area located around Bellur-
80 Nagamangala and Pandavpura cities (Fig.2) may be reliable markers of the reworking and
81 stabilization of this block. Until now, no field, petrological, geochronological and geochemical
82 study have addressed their petrogenesis as well as their significance in the crustal evolution of
83 the WDC. Consequently, the main purpose of this contribution is to 1) constrain the timing of
84 potassic plutonism in Bellur-Nagamangala and Pandavpura regions, 2) decipher their
85 petrogenesis, 3) characterize their relationships with the surrounding basement and, finally, 4)
86 integrate all the results to discuss the whole crustal evolution of the WDC. In order to address
87 all these issues, this study presents field, petrography, zircon U-Pb ages, major and trace
88 element as well as Sm-Nd isotope data for the plutons in Bellur-Nagamangala-Pandavpura
89 corridor (Fig.1 and 2).
90
91 **2. Regional geology of the Dharwar craton**
92 The Dharwar craton preserves a large tilted panel of Archean continental crust with a
93 progressive transition from greenschist in the north to granulite facies in the south
94 corresponding to upper to lower crustal levels, respectively (Fig.1). The craton consists in three
95 main lithological units: 1) TTG-type Peninsular gneisses; 2) volcano- sedimentary
96 greenstone belts formed in two stages (>3.2 Ga old Sargur Group and 3.0-2.6 Ga younger
97 Dharwar Supergroup), and 3) younger calc-alkaline to potassic granites (Jayananda et al.,
98 2018). Earlier studies divided the Dharwar craton into two sub-blocks (western and eastern)
99 separated by the Chitradurga shear zone (Swami Nath et al., 1976; Jayananda et al., 2006;
100 Chardon et al., 2008). More recently, based on the nature and abundance of greenstone-granite
101 patterns, age of the basement rocks, crustal thickness, and distinct thermal records the craton

has been sub-divided into three cratonic micro-blocks (western, central and eastern) (Jayananda et al., 2013a; Peucat et al., 2013; Dey., 2013). In this scheme, the Chitradurga boundary shear zone separates the western and central blocks, and the Kolar-Kadiri-Hungund belts forms the boundary between central and eastern blocks.

The western block consists of a thick (~45 km) crust mainly made up of ca. 3.45-3.23 Ga-old TTG-type Peninsular gneisses (Guitreau et al., 2017; Jayananda et al., 2015) that are tectonically inter-layered with the komatiite-rich Sargur Group greenstone sequences emplaced between 3.38 and 3.15 Ga (Jayananda et al., 2008; Maya et al., 2017). Both lithological units are overlaid by 3.0-2.67 Ga Dharwar Supergroup greenstone sequences that are stratigraphically sub-divided into the Bababudan Group (at the basis) overlain by the Chitradurga Group (Swami Nath and Ramakrishnan 1981). The basis of the Bababudan Group consists in conglomerates, thick basaltic flows (dated at 3.0-2.85 Ga; Kumar et al., 1996) with interlayered quartzite, phyllite and Banded Iron Formations(BIF), at the summit whilst the Chitradurga Group is made up of quartzitic conglomerate, basaltic flows, carbonate, greywacke-argillite, felsic volcanics (dated at 2.67 Ga, Nutman et al., 1996; Jayananda et al., 2013b) and BIFs. All these lithologies were subsequently intruded by 2.62 Ga potassic plutons (Jayananda et al., 2006; Chadwick et al., 2007).

The central block is made of two generations of TTG emplaced at 3.36-3.0 Ga and 2.7-2.56 Ga. The older TTGs contain small interlayered discontinuous bands of high-grade supracrustal rocks whilst the younger transitional TTGs are associated with thin elongated volcanic-dominated greenstone sequences showing bimodal age distribution (2.7-2.67 Ga and 2.58-2.54 Ga (Balakrishnan et al., 1999; Jayananda et al., 2013b). These older TTG greenstone associations intruded by north-south trending calc-alkaline magmatic intrusions. These intrusions are composite magmatic bodies containing voluminous mantle derived juvenile component with minor crustal anatectic melts (Moyen et al. 1997, Moyen et al, 2000,

(Jayananda et al., 2000, 2014; Moyen et al., 2001, 2003a). The most spectacular of those intrusions is the 2.54-2.52 Ga Closepet granite which runs about 500 km from south to the north comprises most abundant juvenile facies of sanukitoid (Martin et al, 2010) affinity and minor anatectic granite (Jayananda et al., 1995; Moyen et al., 2001, 2003).

The eastern block exclusively contains younger transitional TTG, emplaced between 2.7 and 2.55 Ga that are contemporaneous with greenstone sequences (Khanna et al., 2017; Dey et al., 2018; Jayananda et al., 2013a, 2018). Abundant 2.53 Ga-old diatexites together with minor discontinuous calc-alkaline juvenile plutonic bodies emplaced 2.54 Ga ago (Dey et al., 2014; Moyen et al., 2003a). On cratonic scale, strain fabrics mapping and kinematic analysis reveal dome and basin patterns, north trending steep foliations, flat foliations and regional strike-slip shear zones (Bouhallier et al., 1993; Chadwick et al., 2000; Chardon et al., 1996, 1998, 2008, 2011). The whole craton is affected by late-Archean shear deformation which is sub-contemporaneous with emplacement of juvenile plutons and granulite metamorphism that marks the terminal tectonic and thermal event in the central and eastern Dharwar craton (Jayananda et al., 1995, 2000; Moyen et al., 1997, Moyen et al., 2003b; Chardon and Jayananda, 2008; Chardon et al., 2002,2008,2011; Harish Kumar et al., 2003). The three micro-blocks show contrasted thermal histories; medium- to high-pressure assemblages (kyanite-garnet) in the western block; low-pressure and high to ultra-high temperature assemblages (sillimanite-orthopyroxene-spinel-quartz) in the central block, and low pressure and high-temperature (cordierite-sillimanite-andalusite-gedrite and cordierite-spinel) assemblages in the eastern block (Jayananda et al., 2013a). Texturally controlled *in-situ* monazite dating, Sm-Nd garnet-whole rock isochrons as well as SHRIMP U-Pb zircon ages reveal that the western block underwent an early thermal episode at ca. 3.1-3.0 Ga and a major thermal event close to 2.52 Ga, followed by slow cooling to ca. 2.4 Ga (Jayananda et al., 2013a, 2015). The central Dharwar was affected by thermal events at 3.20 Ga and ca. 2.62 Ga, followed by a major high-

grade thermal imprint at ca. 2.54-2.51Ga with cooling up to 2.45 Ga (Jayananda et al., 2011; Peucat et al., 2013). The eastern Dharwar was involved in a widespread thermal event ca 2.52 and 2.51 Ga (Peucat et al., 2013). The distinct thermal records of these three blocks reflect their contrasting accretion histories and their response to late-Archean hot orogen (Chardon et al., 2011).

3. Geology of the studied crustal corridor

The studied area consists of a ~40 km-long north-south crustal corridor adjoining to Sargur Group Nagamangala greenstone belt extending from Mayasandra in the north, through Bellur-Nagamangala to Pandavpura in the south (Fig.2). The dominant lithologies include TTG gneisses, Nagamangala greenstone belt, and potassic plutons. The TTGs mainly consist of medium to coarse grained dark grey tonalite, grey granodiorite, and whitish grey trondhjemite which were affected by strong deformation resulting in a fine banding.

The Nagamangala greenstone belt mainly consists of komatiites to komatiitic basalts, together with minor mafic volcanics and interlayered sediments such as quartzite, pelite, minor carbonate and BIFs (Devapriyan et al., 1994; Tushipokla and Jayananda, 2013). The preserved mineral assemblages correspond to greenschist to lower amphibolite facies conditions (Raase et al., 1986). The granite plutons are mainly found as intrusions either within TTG or along the contact zone between TTG and Nagamangala greenstone belt. Three plutonic bodies have been recognized based on their location and relationship with TTG basement and Nagamangala greenstone belt which include 1) plutons within the TTG basement to the west of greenstone belt 2) plutons in the western and eastern contact zone of the Nagamangala belt and 3) plutons to the south in Pandavpura region (Fig.2).

Pluton within the TTG basement

177 West of Nagamangala greenstone belt, small discrete elliptical granite intrusions are
178 sporadically distributed within the TTG basement. They consist of medium- to coarse-grained
179 dark grey granodiorite and minor whitish grey leucocratic granite; both being cut by coarse-
180 grained pegmatite dykes. The granodiorite occasionally appears as large rounded to pillowed
181 enclave into the leucocratic granite (Fig. 3a); which points towards their contemporaneity.
182
183 *Plutons along the greenstone -TTG contact zone (Bellur-Nagamangala granites)*
184 Bellur-Nagamangala plutons outcrop as elongated massifs or ground-level bouldery exposures
185 which are affected by shear deformation. The deformation of the pluton is more intense along
186 the shear zones or close to the contact with the Nagamangala greenstone belt.
187 Plutons in the western margin contain several facies (Fig. 3b), their field chronology reveals a
188 multi-pulse emplacement, beginning by the intrusion of coarse-grained pinkish to grey
189 porphyritic monzogranite together with highly coarse grained whitish grey monzogranite. This
190 episode has been followed by the emplacement of dark grey quartz-monzonite, grey
191 granodiorite and light grey granite. The coarse-grained whitish grey monzogranite and
192 porphyritic pinkish grey facies are often found as rounded to angular enclaves into both quartz
193 monzonite and granodiorite (Figs. 3c). Dykes of quartz-monzonite with biotite-rich rims are
194 injected into coarse-grained the whitish monzogranite. Such biotite-rim indicates that
195 monzogranite had already started crystallizing at the time of emplacement of quartz-monzonite
196 and granodiorite dykes. Quartz-monzonite, granodiorite and granite often display magmatic
197 flow fabrics (Fig.3d). Occasionally syn-plutonic mafic to intermediate dykes injected into the
198 light pinkish monzogranite to whitish grey granite facies where they show mingling features
199 (Fig.3e). Both dextral and sinistral shear bands traverse all the facies on the outcrop scale
200 where magmatic fabrics are transposed into shear zones (Fig. 3f). In summary, plutons in the
201 western margin, contains several facies which appear to be emplaced in successive pulses

although their time interval may be small as they often show diffusive contacts and magmatic flow structures. Plutons in the eastern margin of the Nagamangala greenstone belt are more homogeneous and contain two main facies including coarse-grained pink and light grey granites. These two facies are often weakly porphyritic, and phenocrysts are stretched. In rare instances, very small biotite rich tiny enclaves (-15 cm) can be found in the granite. They show constrictional fabrics defining L-tectonics with strong horizontal stretching lineation in north-south direction (Fig. 3g).

Plutons in the south (Pandavpura region)

The plutons in the south are found as sporadic intrusions into TTG gneisses along the western boundary of the Chitradurga greenstone belt (see fig.1). These intrusions contain three major facies including coarse-grained whitish grey porphyritic monzogranite, coarse-grained grey granodiorite and light grey granite. Fine-grained dismembered syn-plutonic mafic dykes are found in all the three facies where they frequently contain small rounded enclaves of whitish grey monzogranite (Fig.3h). These plutons are also affected by shear deformation as north-trending dextral and sinistral shear bands traverse different facies on the outcrop scale.

4. Sample description and petrography

This paper is mainly focused on the plutons of both the western and the eastern margin of Nagamangala greenstone belt, which are widespread in the studied corridor (see fig.2).

Granodiorite plutons within the TTG gneisses are fine to medium grained and contain quartz, plagioclase (An_{15-22}), microcline, biotite and, hornblende with rare primary magmatic epidote (Fig. 4a) and accessory zircon, apatite, allanite and opaque minerals.

Among the Bellur-Nagamangala plutons the monzogranites display coarse grained porphyritic to hypidiomorphic granular texture. They contain subhedral to euhedral quartz,

microcline, plagioclase (An_{13-18}), biotite, together with minor bluish-green hornblende containing euhedral primary epidote inclusions (Fig.4b). The epidote is appearing to be an early crystallizing phase as it occurs as euhedral inclusions in hornblende. The common accessory phases are zircon, apatite, allanite, titanite and opaque minerals.

Quartz-monzonite has a medium to coarse grained hypidiomorphic granular texture; it consists of subhedral to euhedral quartz, plagioclase (An_{18-29}), microcline, euhedral primary epidote crystals, bluish-green hornblende and biotite. Accessory phases are zircon, apatite, allanite and opaque minerals. Euhedral epidote crystals are locked as inclusions in biotite with frequent resorbing features that attests of its unstability (Fig.4c). Rarely large broken crystals of magmatic epidote appear as a rim all around allanite crystals.

Granodiorites display medium grained hypidiomorphic granular texture with mineral assemblage including subhedral quartz, plagioclase (An_{18-25}), biotite as well as minor hornblende. Rare euhedral primary magmatic epidote can be found as inclusions in hornblende or biotite (Fig. 4d) whilst secondary anhedral epidote shows symplectic relationships with biotite. Hornblende is bluish-green which is unstable being rarely replaced by biotite. Further, it appears that late stage fluids reacted with hornblende and feldspars, which resulted in the development of secondary epidote.

Granites in the eastern margin of Nagamangala greenstone belt show medium to coarse grained with hypidiomorphic granular to weakly porphyritic texture. They contain quartz, abundant microcline, minor plagioclase (An_{10-14}), biotite and occasional primary muscovite. Euhedral primary magmatic epidote often show resorbing features whilst anhedral secondary epidote show symplectic relationship with biotite. Primary epidote rarely forms a rim to allanite.

The general texture of the studied plutons is often anisotropic due to shear deformation. Close to the shear zones, the grain size progressively decreases, which militates in favor of a

252 ductile deformation. Medium to fine grained quartz-monzonite and granodiorite often display
253 bimodal grain size with large subhedral to euhedral quartz and feldspar crystals and small
254 subhedral to euhedral quartz and K-feldspar crystals. Such features could be interpreted in
255 terms of quench texture resulting of the rapid ascent and fast cooling of the pluton. Larger
256 subhedral to euhedral quartz crystals also contradict slow cooling and substantiate rapid ascent
257 of the magma, possibly as dykes into higher levels in the crust which could avoid complete
258 resorption of epidote.
259 In summary these plutons contain primary magmatic epidote and show evidence for a rapid
260 cooling.

261 The Pandavpura plutons are medium to coarse grained and show equigranular to porphyritic
262 texture. They contain quartz, microcline, plagioclase (An12-17), biotite, rare hornblende with
263 accessory zircon, titanite and opaque minerals.

264 Among the studied plutons nine samples were selected for zircon U-Pb geochronology
265 whose petrographic characteristics are presented below.

266

267 *Sample MS05: Granodiorite*
268 Sample MS05 collected from a small plutonic body intrusive into the TTG basement west of
269 Nagamangala greenstone belt about 6 km west of Mayasandra village. The rock shows medium
270 grained hypidiomorphic granular texture and contain quartz, plagioclase (An_{18-20}), microcline
271 (subordinate), biotite and minor hornblende with accessory zircon, apatite, titanite and opaques.
272 It contains euhedral primary magmatic epidote inclusions in hornblende. The magmatic epidote
273 in turn contains inclusions of zircon (see fig.4a).
274 *Sample NM 04 - Granodiorite*

This sample is a granodiorite collected from a small intrusion in TTG basement about 4 km southwest of Nagamangala town. It displays medium to fine grained hypidiomorphic texture, where, due to deformation minerals are aligned into the foliation plane. It contains quartz, plagioclase (An_{18-23}), subordinate microcline, hornblende and biotite with accessory zircon, apatite, titanite and Fe-Ti oxides.

Sample AC01: Quartz monzonite

Sample AC01 collected from an abandoned quarry close to Adichunchanagiri temple entrance gate in Bellur-Mayasandra road. The sample exhibits medium to coarse hypidiomorphic granular texture. It contains quartz, plagioclase (An_{17-23}), microcline, primary epidote, bluish-green hornblende, biotite with accessory zircon, apatite, titanite and opaque minerals. Primary epidote found as euhedral crystals within hornblende. Primary epidote is often unstable and resorbed during emplacement.

Sample BH 50c - Porphyritic monzogranite

It is a coarse grained porphyritic monzogranite sampled from the western boundary of the Nagamangala greenstone belt that outcrops in the western outskirts of Nelligere village. The mineralogy includes quartz, plagioclase (An_{15-20}), microcline, magmatic epidote (some grains could be secondary), hornblende, biotite with accessory zircon, allanite, titanite and Fe-Ti oxides. Magmatic epidote found as euhedral inclusions in hornblende and biotite. Constituent minerals show strong orientation but no evidence for grain size reduction as corroded boundaries not observed.

Sample CHT2 – Pink granite

Sample CHT 2 is a medium to coarse grained granite that shows bimodal grain size and contains quartz, microcline, plagioclase (An_{10-12}), biotite and traces of primary epidote. Quartz occur as large elongated grains (phenocrysts?) as well as fine grained aggregates. This could be either quench texture resulting by rapid emplacement and cooling of magmas or resulted through progressive grain size reduction during deformation. Microcline is dominant over plagioclase. Biotite is the major ferromagnesian phase, which together with few grains of primary epidote and accessory phases forms cluster. Zircon, apatite, allanite titanite and magnetite are common accessory minerals found as inclusions or interstitial phases.

Sample 5-J-5 – Light grey granodiorite

The sample collected from a quarry along the western boundary of the Nagamangala greenstone belt about 5 km north of Bellur in Mayasandra road. The sample show medium grained hypidiomorphic granular texture; it consists in an assemblage of quartz, plagioclase (An_{16-20}), microcline, biotite with zircon, apatite, titanite and opaques as accessory phases.

Sample 5-T48b – Pinkish monzogranite

The sample collected in Yediyur-Mayasandra road close to the northern terminus of the pluton in the eastern side of Nagamangala greenstone belt (about 6 km SE of Mayasandra). It is coarse grained showing hypidiomorphic granular texture. The mineral assemblage include quartz, plagioclase (An_{14-18}), microcline, small magmatic epidote crystal inclusions in biotite and accessory phases like zircon, apatite, allanite, titanite and Fe-Ti oxides.

Sample PAN 01- Porphyritic monzogranite

The sample is collected from an active quarry about 2 km southeast of Pandavpura town. It shows coarse grained porphyritic texture with bimodal grain size. The mineral assemblage include quartz, plagioclase (An_{15-18}), biotite with accessory zircon, apatite, titanite and opaque phases.

Sample PAN 02 – Quartz monzonite

The sample collected in a large quarry about 3 km NE of Pandavpura town. It shows coarse grained hypidiomorphic granular texture and contains quartz, plagioclase (An_{18-25}), hornblende, biotite with accessory zircon, apatite, titanite and opaque phases.

5. Analytical methods

5.1. Zircon U-Pb geochronology

Zircon U-Pb isotope analyses were performed by secondary-ionization mass-spectrometry (SIMS) and by laser-ablation inductively-coupled-plasma mass-spectrometry (LA-ICP-MS). SIMS analyses were carried out using the CAMECA 1270 ion microprobe at the CRPG, CNRS-Nancy (http://www.crpg.cnrsnancy. fr/1270). Procedures are described in Deloule et al. (2002). Uncertainties for individual analyses (ratios and ages) are given at 1σ level, but the uncertainties in calculated weighted mean ages are reported at 2σ. All ages were calculated using the decay constants and isotopes abundance listed by Steiger and Jager (1977). Errors on ages are quoted at 2σ and were calculated using the Isoplot program of Ludwig (2001).

Zircon U-Pb geochronology by LA-ICP-MS was done at Laboratoire Magmas et Volcans (LMV), Université de Clermont Auvergne, Clermont-Ferrand (France). Prior to dating, zircon crystals were handpicked and mounted in epoxy. We selected the most euhedral, pale pink and clear crystals with no or the least inclusions possible. Zircon crystals were further

polished to their approximate center and imaged by cathodoluminescence at Laboratoire Magmas et Volcans (LMV) using a Jeol JSM-5910LV scanning electron microscope. Images were acquired using an acceleration voltage of 15kV. The zircon internal textures were used to select the least radiation-damaged crystals and to determine the locus for U-Pb dating. We prioritized bright zones that show fine-oscillatory zoning as they correspond to pristine magmatic domain that are likely to reveal accurate crystallization ages (Corfu et al., 2003)

Operating conditions during the LA-ICP-MS analyses are given in Table 1. LA-ICP-MS analyses were conducted by standard-bracketing using the zircon standard 91500 (1065 Ma; Wiedenbeck et al., 1995) for external normalization. The zircon standards AS3 (1099 Ma; Paces and Miller, 1993) and Plesovice (337 Ma; Sláma et al., 2008) were further used for data quality control. Data were processed using GLITTER software package (Van Achtenberg et al., 2001) and further plotted using ISOPLOT version 3.75 (Ludwig, 2008). Semi-quantitative concentrations were also calculated from the measured signals by external normalization to 91500. U-Pb analyses gave a concordant age of 1092 ± 6 Ma (2σ; MSWD = 0.43; n = 13) and a weighted average $^{207}Pb/^{206}Pb$ age of 1092 ± 7 Ma (2σ; MSWD = 0.17; n = 15) for AS3, as well as a concordant age of 328 ± 6 Ma (2σ; MSWD = 1.8; n = 13) and a weighted average $^{207}Pb/^{206}Pb$ age of 335 ± 7 Ma (2σ; MSWD = 0.83; n = 13) for Plesovice. The obtained ages for zircon standards are, thus, in good agreement with consensus ages uncertainty-considered. The average U, Th, and Pb concentrations obtained for AS3 were 256, 164 and 63 ppm, which are consistent with those measured in Paces and Miller (1993). The average U, Th, and Pb concentrations obtained for Plesovice were 585, 52 and 34 ppm, which are consistent with those measured in Wiedenbeck et al. (1995). Results for zircon standards are presented in Table 3

5.2 Whole-rock major and trace element analyses

CHT and BH series samples were crushed using agate mill at Geosciences Rennes, Université de Rennes 1 (France) and analysed using Philips XRF, whereas all other samples were crushed in Japan using Agate mill and analysed for major and trace elements by using fully automated XRF (Rigaku RIX 3000) at centre of instrumental Analysis, Yamaguchi University by glass beads method ($Li_2B_4O_7$ as *spectromelt*). Details of analytical methods for major and trace elements using XRF at Rennes and Yamaguchi is already reported in Jayananda et al. (2006, 2008)

The full range of trace elements for CHT and BH samples were analysed by ICP-AES and ICP-MS, respectively at CRPG, Nancy with analytical procedures described at http://www.crpg.cnrs-nancy.fr/SARM. For trace elements, precision is better than 5%; for contents less than 30 ppm the uncertainties are within 10% and for elements with concentration less than 5 ppm uncertainty is in the range of 10–50%. Other samples were analysed by using Quadrupole ICP-MS at CSIR-National Geophysical Research Institute, Hyderabad. Analytical procedures for trace element analysis using ICP-MS are presented elsewhere (Satyanarayanan, et al., 2018).

5.2. Nd isotopes

Nd isotope compositions for whole-rocks were determined using a Finnigan Mat 262 mass spectrometer at Geosciences Rennes. Total blanks for Sm and Nd contents were lower than 0.05 ng. Uncertainties on $^{147}Sm/^{144}Nd$ ratios were estimated at 0.2%. Replicate analyses of La Jolla standard yielded a mean $^{143}Nd/^{144}Nd$ ratio of 0.511857 ± 3 in agreement with the consensus value. Details of aanalytical protocols for Sm-Nd separation, standards used, and instrumentation conditions are already presented in Jayananda et al. (2015). Epsilon Nd values were calculated using the CHUR values provided in Bouvier et al. (2008).

6. Results:

6.1. Zircon U-Pb geochronology

6.1.1. Sample MS-05

Zircon crystals from this sample show simple oscillatory zoning among studied samples. However, many zircon grains are subhedral to round. Dark outer-rims are also present around some crystals. A few zircon grains, show a core surrounded by an oscillatory-zoned outer part. Most of the analysed crystals had modest U and Th contents below 200 and 100 ppm, respectively. Th/U range from ~0.1 to 0.6, much like zircons from NM-04. Fig. 5a illustrates the more complex nature of U-Pb data acquired on MS-05 zircon crystals than on other samples studied herein (Table 3). Graphically, two *discordia* lines are defined by the data point which is mirrored in the dichotomous distribution of $^{207}Pb/^{206}Pb$ ages. When most concordant zircons are considered, two Concordia ages (Fig. 5a) are obtained: 3310 ± 10 Ma (2σ; MSWD = 0.039) and 3210 ± 10 Ma (2σ; MSWD = 0.35). These ages both correspond to zones that exhibit fine oscillatory zoning, and, in the light of internal textures, we interpret the former to correspond to inherited cores and the latter as the age of crystallization of the rock.

6.1.2. Sample NM-04

Zircon crystals from NM-4 show simple oscillatory zoning that is not concentric in CL images. Studied crystals were subhedral and slightly elongated (Fig. 5b). Most crystals have moderate U and Th contents of 100-200 and 50-100 ppm, respectively. Th/U are lower than those seen in zircons from other samples as they range from 0.1-0.7. Determined $^{207}Pb/^{206}Pb$ ages are consistent between all crystals in spite of variable degrees of discordance (Table 3). When most concordant analyses are considered, a concordia age of 3205 ± 8 Ma (2σ; MSWD = 0.69) is obtained (n=3) (Fig. 5b) that dates this sample.

6.1.3. Sample AC01:

Zircon crystals have variable habits from roughly euhedral to xenomorphic (Fig. 5c). Internal textures are commonly complex with patches of bright domains within which partly distorted oscillatory zoning can be seen. Other domains appear either dark and homogeneous, or dark with broad zoning. The distribution of bright and dark domains gives the impression that original fine oscillatory zoning had been disturbed and that zircon partly recrystallized in places. Most zircon grains exhibit moderate to slightly elevated U and Th contents of 100-400 and 40-200 ppm, respectively (Table 3). These crystals show a large range of Th/U from 0.09 to 1.08 that correlate with the degree of discordance of U-Pb ages. U-Pb data are concordant to limitedly discordant and align along a single *discordia* line. The most concordant U-Pb data give a *concordia* age of 2981± 8 Ma (2σ; MSWD = 0.45; n = 4) that is interpreted as magmatic crystallization (Fig.5c).

6.1.4. Sample BH-50

Most zircon grains exhibit fine oscillatory zoning in BSE images (Fig. 5d). Some crystals have rounded cores surrounded by overgrowths. U and Th concentrations vary from low (e.g., <100 ppm for U) to moderate (e.g. ~300 ppm for U). U-Pb data define two major groups as illustrated by the data distribution in a concordia diagram (Fig. 5d). An older group with a weighted average $^{207}Pb/^{206}Pb$ age of 3220 ± 10 Ma (2σ; MSWD = 4.5; n= 3; Fig. 5d) and a younger group that define a *discordia* line identical to that formed by CHT-2 zircons (Fig.6e) and that overall give an upper-intercept age of 2982 ± 11 Ma (2σ; MSWD = 5.; n = 9; see Fig. 5d). The older group corresponds to the cores identified whereas the younger group is found both in some oscillatory domains and in overgrowth around rounded cores. Th/U ratios vary from 0.2 to 1.8 and are broadly inversely correlated with determined $^{207}Pb/^{206}Pb$ ages so that the lower and higher Th/U correspond to respectively the oldest and the youngest group. As a consequence, we interpret the youngest age (2982 ± 11 Ma) as that of crystallization of BH-50 given that oldest age corresponds to inherited cores.

447 6.1.5. Sample CHT-2

448 Zircon crystals are euhedral to subhedral and exhibit oscillatory zoning (Fig. 6e). They have
449 moderate to relatively high U and Th content (Table 2) as well as Th/U between 0.5 to 1.3. U-
450 Pb data are concordant to significantly discordant and essentially align along a single *discordia*
451 line (Fig. 5e). The most concordant data give a *concordia* age of 2989 ± 84 Mae (n = 2; MSWD
452 = 1.5), which is consistent with all $^{207}Pb/^{206}Pb$ ages but that of a discordant data point. We
453 interpret the *concordia* age to date the magmatic crystallization of CHT-2 sample.

454 6.1.6. Sample 5-J-5

455 Only few zircons were recovered from this sample and most of them showed advanced
456 radiation damage. Consequently, we analysed 5 zircon crystals but only present 4 analyses for
457 this sample, as one zircon contained measurable amounts of common Pb. Zircon crystals are
458 stubby to slightly elongated, generally euhedral and with simple oscillatory-zoning from core
459 to rim as revealed by CL images (Fig. 5f). Most zircon cores appear brighter than their
460 surrounding outer growths, though without visible truncation of the zoning. Darker growth
461 bands in CL images reveal that these crystals underwent advanced amorphization in places.
462 This is consistent with the fact that most crystals have U and Th concentrations slightly beyond
463 400 and 200 ppm, respectively, and the degree of discordance of the U-Pb ages increases with
464 increasing U and Th concentrations. In spite of these issues, all measured $^{207}Pb/^{206}Pb$ ages are
465 essentially consistent (Table 3), within error, with the least discordant data, which is explained
466 by the fact that all data points define a broadly simple *discordia* line that passes through the
467 origin (i.e., 0 Ma). If we use the least discordant U-Pb data, an age of 2974 ± 13 Ma (2σ; Fig.
468 5f) is obtained, which is identical to that of the least discordant zircon (Table 3; Fig.5f). We
469 purposely excluded the most discordant data in age calculation as they are known to reduce the
470 accuracy of age establishment in addition to possibly introduce noise in age calculation
471 (Guitreau and Blichert-Toft, 2014). Th/U range from 0.6 to 1.

472 6.1.7. Sample 5-T48b

473 Zircon crystals from this sample generally display fine oscillatory-zoning. They are stubby to
474 slightly elongated and have euhedral to subhedral shapes (Fig.5g). A very thin and bright rim
475 can be seen around most crystals and appear to be coating partly resorbed margins. Some
476 crystals have euhedral cores surrounded by a thin and uneven outer part it self-surrounded by
477 an outer growth that exhibit oscillatory zoning. U and Th concentrations in these zircon crystals
478 are almost all below 200 and 100 ppm, respectively, and Th/U ratios range from 0.5 to 1. All
479 determined $^{207}Pb/^{206}Pb$ ages are essentially consistent despite various degrees of discordance
480 (Table 3). This is accounted for by the fact that data points define a simple *discordia* line in a
481 plot that passes through 0 (Fig. 5g). The four most concordant data give a concordia age of
482 2984 ± 8 Ma (2σ; MSWD = 0.2; Fig. 5g) which we interpret as the crystallization age of this
483 sample.

484

485 6.1.8. Sample PAN-01

486 Zircon crystals are limitedly elongated, euhedral to slightly subhedral, and exhibit simple and
487 fine-oscillatory zoning. Some resorbed cores can be visible in some crystals as well as distorted
488 oscillatory zoning (Fig. 5h). Most zircon crystals have U concentrations below 200 ppm and
489 Th concentrations below 100 ppm thereby indicating that they likely underwent limited alpha-
490 decay damaging of their lattice which can significantly affect U-Pb isotope systematics (e.g.,
491 Guitreau et al., 2018). Th/U ratios displayed by PAN-01 zircons range from 0.5 to 1.
492 Determined U-Pb ages are fully concordant to limitedly discordant and very consistent between
493 all analysed crystals (Table 3). Data form a simple population in a Concordia plot (Fig. 5h)
494 with a calculated *concordia* age of 2598 ± 6 Ma (2σ; MSWD = 1.07; n = 13) that dates the rock
495 formation.

496

6.1.9. Sample PAN-02

Zircon crystals from PAN-02 are very similar to those from PAN-01 as they are limitedly elongated, euhedral to subhedral, and exhibit simple and fine-oscillatory zoning. Core resorption can be seen in some crystals, as well as distortion of fine oscillatory-zoning in rounded cores (Fig. 5i). A few crystals also contain inclusions of small zircon (≤10 µm). Most zircon crystals have U concentrations below 100 ppm and Th concentrations below 70 ppm. Th/U ratios displayed by PAN-02 zircons range from 0.3 to 1.1. Determined U-Pb ages are almost all fully concordant and very consistent with each other (Table 3). This simple population gave a *concordia* age of 2608 ± 7 Ma (2σ; MSWD = 1.5; n = 11; Fig. 5i) indicative of PAN-2 crystallization.

6.2. Whole rock geochemistry

Major and trace element data are presented in Table 4. All major element analyses were recalculated on an anhydrous basis, with iron expressed as Fe_2O_3*= Fe_2O_3 + 1.111 FeO.

6.2.1. Major elements

The studied plutons display a wide range in SiO_2 contents (63.89 to 76.47 wt. %), with high Na_2O+K_2O (average = $\bar{x}$ = 8.12 wt. %), and high K_2O/Na_2O (typically>1 with $\bar{x}$ = 1.08). Their relative K-enrichment make them drastically different of the Archean TTGs into which they intruded in the western Dharwar craton (Fig.6a). Another chemical characteristic of these rocks is their moderately low (Fe_2O_3*+MnO+MgO+TiO_2; $\bar{x}$ = 4.04 wt. %), which associated with a very low Mg# ($\bar{x}$ = 0.28; Mg# = molecular Mg/(Mg+Fe)), points to their high degree of differentiation. The magmatic suite is mainly made of monzogranite and followed by granodiorite and minor syenogranite (Fig. 6b).

In the A/NK versus A/CNK diagram (Fig.7; Shand, 1943), the studied granites fall into both the metaluminous and peraluminous fields.

In the normative Q-Ab-Or triangle, after Blundy (2001) and adapted from Tuttle and Bowen, (1958), the studied granites have compositions that plot close to the minima on the quartz-feldspar cotectic in an 'hydrous granitic system' for pressures ranging between 2 and 10 kb (Fig.8).

On Harker binary diagram (Fig 9), all the major elements, except K_2O, are negatively correlated with SiO_2. As the content of SiO_2 can be higher than 76 wt.%, the negative correlation could be attributed to a sum effect. However, such an effect would affect all elements at the same degree, which is obviously not the case especially for K_2O that is positively correlated with SiO_2.

6.2.2. Trace elements

Most trace elements correlate with SiO_2 content, used here, as differentiation index (Fig.10). On binary diagrams Rb and Ba (despite relative scattering of data) are positively correlated with SiO_2, whilst other elements such as Sr, Ni, Cr, V, Zr, Nb and Y display moderate to weak negative correlation. In all trace element versus SiO_2 plots, data always fall on a single straight trend and do not show any inflexed or broken line.

The ca. 3.2 Ga granodiorite samples contain moderate total REE (117-119 ppm), display moderately to strongly fractionated patterns (Fig. 11a) [$(La/Yb)_N$ = 13.75 -21.74] without any Eu anomalies (Eu/Eu* = 0.89-0.97). These patterns are similar to those of the associated TTGs except that they are HREE-richer (see fig. 11a) which could be attributed to absence of significant amounts of residual garnet during melting. The ca.3.0 Ga Bellur-Nagamangala granites exhibit large variations in REE abundances (total REE ranging from 101 to 826 ppm). No one REE shows strong correlation with SiO_2 but total REE roughly decrease

546 with increasing SiO_2. Based on the total REE contents the granites are divided into three
547 groups: EE.

548 The group 1 corresponds to leucocratic pink to whitish grey granite facies which generally
549 contain low to moderate ΣREE (101-179 ppm) contents and show moderate to strongly
550 fractionated REE patterns [$(La/Yb)_N$ = 10.14-50.39)] with negative Eu (Eu/Eu*=0.28-0.65)
551 anomalies (Fig. 11b).

552 The group 2 consists of coarse-grained to weakly porphyritic light pink monzonite. It has
553 high ΣREE (205-392 ppm) contents and moderate to strongly fractionated REE patterns
554 [(La/Yb_N) = 6.86 – 34.02] together with negative Eu (Eu/Eu*=0.35-0.61) anomalies (Fig.11c).

555 The group 3 corresponds to medium- to coarse-grained quartz-monzonite with few
556 samples of porphyritic grey monzonites. They have very high ΣREE contents (429-826 ppm).
557 They show moderate to strongly fractionated REE patterns [[(La/Yb_N)= 8.63 – 29.53] with
558 strong negative Eu (Eu/Eu*=0.30-0.54) anomalies (Fig. 11d).

559 The ca. 2.6 Ga Pandavpura granites display high to very high total REE contents (479-689
560 ppm) with moderately fractionated REE patterns [$(La/Yb)_N$ = 5.88-9.89)] and strong negative
561 Eu (Eu/Eu*= 0.10-0.11) anomalies (Fig.11e) .

562 When plotted in a $(La/Yb)_N$ versus Yb_N diagram, the studied granites does not show any
563 affinity with typical Archean TTG and plot in the field defined Phanerozoic calc-alkaline
564 granitoids (Fig.11f Martin, 1986). In summary, the granite REE patterns militate in favour of
565 plagioclase fractionation during magmatic differentiation or as residual phase during the
566 melting event. They also preclude any role played by,garnet in the source residue.

567 On primitive mantle (Sun and McDonough, 1989) normalized multi-element diagrams all
568 the three groups of plutons (Fig. 11g-k) uniformly show negative anomalies of Ba, Sr, Nb, Ta,
569 which appear consistent with the fractionation of plagioclase, ilmenite and/or rutile. Flat HREE

570 pattern together with slight positive Y anomalies preclude role of residual garnet during partial
571 melting of the source.
572
573 **6.3. Sm-Nd isotope geochemistry**
574 The analyzed granitoids display a relatively large range in $^{147}Sm/^{144}Nd$ (0.083-0.1413) and
575 present-day $^{143}Nd/^{144}Nd$ (0.510354-0.511510; Table 5) and these two parameters are positively
576 correlated. The slope of this correlation in a $^{147}Sm/^{144}Nd$ versus $^{143}Nd/^{144}Nd$ plot is 0.0195 ±
577 0.0015 (2σ) which corresponds to an age of 2953 ± 225 Ma (2σ). The large uncertainty on this
578 slope is due to excess scatter around the correlation. If the two most dispersed data points are
579 removed, the slope becomes 0.0196 ± 0.0008 which translates into an age of 2977 ± 115 Ma
580 (2σ; Fig. 12a). Both ages mentioned above, though imprecise, are consistent with those
581 determined by zircon U-Pb geochronology for samples CHT-2 and BH-50 that are part of the
582 Sm-Nd correlation in Figure 12a. We have, therefore, calculated initial Nd isotope
583 compositions at 3000 Ma and they show a range from 0.508659 ± 0.000005 (2σ) to 0.508774
584 ± 0.000004 (2σ), which correspond to respective ε_{Nd} values of +0.5 ± 0.1 and -1.7 ± 0.1 (2σ).
585 It is interesting to note that initial Nd isotope compositions correlate with major and minor
586 oxide concentrations such that $^{143}Nd/^{144}Nd(t)$ is negatively correlated with SiO_2 (Fig. 12b) and
587 K_2O, for instance, and positively correlated with MgO, CaO, ZrO_2 and TiO_2.
588 In this study we have analyzed only 3.0 Ga plutons for Nd isotopic compositions and Sm-Nd
589 isotope data presented in the Table 5. The analyzed samples show Nd model ages ranging
590 3379 Ma to 3183 Ma and $\varepsilon_{Nd\ (T=3.0\ Ga)}$ ranging -2.0 to -0.7 except one sample showing +0.2
591 suggesting dominant crustal source with possible minor juvenile input in their genesis. These
592 values are close to the values obtained for the TTG gneisses further west, in the eastern part of
593 the Holenarsipur greenstone belt and immediately north in Tiptur-J.C.Pura region (Chardon,
594 1997).

7. Discussion

7.1. Timing of potassic magmatism with respect to TTG accretion in Western Dharwar Craton (WDC)

In the Western Dharwar craton, the TTG protoliths emplaced during three major episodes: ca. 3600 Ma, 3450-3300 Ma and 3200 Ma (Meen et al.,1992; Peucat et al., 1993; Iswar Kumar et al., 2013; Jayananda et al., 2015; Guitreau et al., 2017). Sporadic plutons with compositions transitional between TTG and potassic granites (e.g Chikmagalur granodiorite and other small intrusions west of Holenarsipur) dated ca. 3150 Ma correspond to the last juvenile magmatic event in this area, thus underlying the transition towards potassic magmatism started at ca. 3000 Ma. Samples NM04 and MS05 as well as the zircon cores of BH50 belong to this early magmatic history of the WDC ca. 3200 Ma which coincides with the emplacement of diapiric trondhjemites further west in Holenarsipur region (Jayananda et al., 2015). Samples PAN-1 and PAN-2 have younger crystallization ages of ca. 2.6 Ga, similar to other known potassic granites such as Arsikere-Banavara and Chitradurga granites located further to the north of the corridor (Jayananda et al., 2006).

The Bellur- Nagamangala granites yield zircon U-Pb ages of ca. 3000 Ma. These ages are similar to those of granite plutons outcropping immediately north in Tiptur region (Chardon, 1997) and Bukkapatna granite further north east (Chardon et al., 2011), Karwar granite (Iswar Kumar et al., 2013) and few discrete plutons in the north-western part of the Dharwar craton. Consequently, the ages presented in this paper, together with published data show that juvenile TTG accretion contributing to major crustal growth occurred in successive stages ca. 3.6 Ga, 3.45-3.3 Ga and 3.2 Ga (Jayananda et al., 2015; Guitreau et al., 2017) whilst potassic granite emplacement corresponding to episodes of crustal reworking took place at ca. 3.2-3.15 Ga, 3.0 Ga and 2.6 Ga. This contrasts with the central to eastern blocks of the Dharwar

620 craton where major outbursts of juvenile crust accretion and crustal reworking led to the
621 emplacement of sanukitoids as well as anatectic potassic granites during 2.56-2.52 Ga followed
622 by cratonization ca. 2.5 Ga (Moyen et al, 1997, 2001, 2003; Peucat et al., 1993; Chardon et al.,
623 2011; Jayananda et al., 1995, 2000; Dey et al., 2016).
624
625 *7.2. Petrogenesis and sources*
626 The major focus of this section is to address the petrogenetic history of 3.0 Ga Bellur-
627 Nagamangala plutons as most of the data presented in this paper refer to those plutons. On the
628 other hand, some observations on petrogenesis are also made on the 3.2 Ga and 2.6 Ga
629 intrusions.
630 7.2.1. 3.2 Ga Granodiorite
631 These granodiorites form sporadic intrusions within TTG basement to the west of
632 Nagamangala greenstone belt. They are metaluminous and plot within the main trend of 3.0
633 Ga plutons on Harker's binary plots, Ab-An-Or triangular plots (see Figs. 6 and 9). Their
634 moderately fractionated REE patterns are similar to TTG except that they with slightly higher
635 HREE together with low Cr/V ratios, preclude garnet in the melt residue. The REE patterns
636 without any Eu anomalies could be attributed to simultaneous crystallization of hornblende and
637 plagioclase. These granodiorites show a transitional character from TTG to high potassic
638 granites as reflected on $(La/Yb)_N$ *vs.* (Yb). In view of above arguments, it can be concluded
639 that the ca. 3.2 Ga granodiorite probably originated by melting of mafic crust under water
640 saturated conditions.
641 *7.2.2. 3.0 Ga Bellur-Nagamangala plutons*
642 Field evidence for emplacement of granites as dykes/sheets together with rounded enclaves of
643 more felsic facies into intermediate to mafic facies with sharp to diffusive contacts and
644 mingling features show that felsic and intermediate facies interacted during crystallization and

emplacement. This is supplemented by the fact that all the facies have the same ca. 3.0 Ga age. The whole rock geochemistry particularly correlations observed on Harker's binary plots indicate that the plutons result of interaction (mixing and/or mingling) between two components; one being SiO_2-rich whilst the other has intermediate composition. This behavior, over a wide range of SiO_2 cannot be accounted for only by pure fractional crystallization because changes in crystallizing phases usually lead to broken or curved trends. By contrast, a process involving interaction, mixing and mingling of two end-member magmas undergoing fractional crystallization is more likely responsible for such straight lines (Janoušek *et al.*, 2015). This is also evidenced by the fact that Nd isotope signatures calculated at 3.0 Ga negatively correlate with SiO_2 content (Fig. 12b).

7.2.3 Felsic end-member

Field chronology indicate that felsic end member like whitish to light pink granite and monzogranite emplaced during early in the magmatic historyof 3.0 Ga plutons and possibly generated by crustal melting in lower part of the middle crust under water saturated conditions as revealed by Q-Ab-Or granite system (see Fig.8). Major and trace elements (Fig. 9 & 10) clearly show that the felsic end-member has no TTG affinity but is rather granitic (felsic) in composition. Similarly, the contacts between felsic and intermediate granitoids are often rounded or lobated, demonstrating that they interacted while they were still liquid or better as a magmatic mush (Barbarin and Didier, 1992; Hallot *et al.*, 1996; Jayananda et al., 2009,2014).

On the other hand, many samples of the felsic end-member have A/CNK >1 but normative corundum always lower than 1% ($\bar{x}$ = 0.35%); they are metaluminous to peraluminous. This characteristic precludes a possible origin entirely by melting of aluminium-rich sediments, such as the kyanite-rich pelitic sediments exposed in the surrounding Nagamangala greenstone belt. Consequently, a more realistic alternative scenario would be

direct partial melting of the TTG basement without or with small amounts of Al-rich sediments. This would be consistent with Nd isotope signature of Peninsular gneisses further west and north as they would exhibit ε_{Nd} between -0.6 and -3.7 at 3.0 Ga (Chardon, 1997; Jayananda et al. ,2015).

Figure 11 shows that HREE patterns for all the three groups of the Bellur- Nagamangala granites are limitedly fractionated with an average $(Gd/Yb)_N = 0.62 – 2.62$ (except one sample 3.38 and high $Yb_N = 14.6$. Contrastingly, TTGs have fractionated HREE: $(Gd/Yb)_N = >3.1$ with low $Yb_N = 3.0$. Assuming that the felsic end-member is generated by partial melting of TTGs would preclude garnet as a residual phase as indicated by HREE and Y on multi-element diagrams. Indeed, the TTG source has low Yb content while the Bellur-Nagamangala granites have higher Yb contents, in other words, Yb should have behave as a strongly incompatible element. In felsic liquids, $Kd_{Yb}^{garnet/liquid}$ varies between 35 and 40, which results in a compatible behaviour of Yb. Therefore, a magmatic liquid in equilibrium with residual garnet will be depleted in Yb, whereas exactly the opposite is observed in the studied granites. Consequently, the felsic end-member could have been formed by partial melting of the TTG basement in the absence of garnet which, hence, indicate pressures lower than 12 kb which is the pressure of apparition of garnet in the TTG mafic source (Schmidt and Poli, 2004).

In the Bellur- Nagamangala granites the average K_2O content is 4.17 wt%, while it is only of 1.93 wt% in average TTG (Martin *et al.*, 2005). So, potassium must have had an incompatible behaviour during TTG melting. Experimental melting of felsic rocks shows that biotite is one of the most frequent residual phase. Assuming a K_2O content of 9.5 wt% in magmatic biotite, allows to fix a maximum degree for partial melting: it ranges from 46% for a biotite free residue down to 0% for a residue containing 20.3% biotite. Indeed, it is possible to overtake this limitation, by considering biotite incongruent melting, which result in the formation of a K_2O-free new residual phase such as orthopyroxene.

In summary, the SiO_2-rich component of the Bellur-Nagamangala granites is consistent with partial melting of the TTG basement at pressure lower than 12 kbars.

7.2.4 Mafic to intermediate end-member for mixing/mingling

The silica poorer quartz-monzonite to monzodiorite-dioritic samples of the Bellur-Nagamangala plutons contain abundant hornblende, which together with high REE and Nd isotopes (εNd_T = 0.2 to -0.4) point towards juvenile input from possibly enriched mantle. However, the lowest silica content (63.89 wt.%) of studied rocks together with their lower Mg# < 0.45 is not consistent with direct melting of the mantle. One way to reconcile these contradiction is to consider that the intermediate component corresponds to a mantle-derived melt that evolved through fractional crystallization and/or contamination within the continental crust. Consequently, we can reasonably assume a mantle origin for the SiO_2-poor component. Similar situation was proposed for the Closepet granite wherein the mantle derived magma have evolved through fractional crystallization (Moyen, 1997; Moyen *et al.*, 2001). An alternative assumption would be that the intermediate compositions result from mixing with the felsic end-member. This latter hypothesis would be consistent with the near-CHUR Nd isotope signature of the intermediate end-member given that more depleted sources are known in the WDC (e.g., Dey, 2013).

An important issue is that, except for K_2O, Rb and Ba, all elements negatively correlate with SiO_2. Consequently, the mafic end-member was alreadyriched in incompatible elements, which implies that its mantle source was also enriched. Alternatively, fractional crystallization of a mantle-derived melts, with possible crustal contamination, would also account for the enrichment of the mafic-intermediate end-member.

7.2.5 Model for the origin of 3.0 Ga Bellur-Nagamangala plutons

720 Field evidence, petrographic characteristics together with elemental data reveal that the Bellur-
721 Nagamangala plutons were generated 3.0 Ga ago by interaction between two contrasted end
722 members: one being the mantle and the other the TTG basement. We propose that a mantle-
723 derived magma emplaced into a hot TTG crust, with which it mixed and/or mingled. The
724 heating of the crust could possibly result of the emplacement of the hotter mafic magmas.
725 induced the melting of TTGs at lower crustal levels. Rough pressure estimates indicate that
726 melting of the TTG crust likely occurred below pressures of 12 kb to account for the absence
727 of garnet in the residue, but in the range of ~2 to 10 kb as shown by cotectic melts in a hydrous
728 granite system (Fig. 8). This is further substantiated by the high-HREE and moderately to
729 poorly fractionated REE patterns and 1/Er – (Ba+Sr)/1000-Er (Heilimo et al., 2010) triangular
730 plot (Fig.13).
731 The presence of magmatic epidote in the studied granites allow us to constrain further the depth
732 of melting and crystallization of these magmas. Indeed, the experimental work of Naney
733 (1983) on crystallization sequence ingranodioritic magmas shows that at 2 kbar epidote did not
734 crystallize whilst at 8 kbar under low water activity orthopyroxene formed. The, magmatic
735 epidote and hornblende crystallized at 700-600^{o}C with increasing H_2O activity Subsequent
736 experimental work on melting and crystallization of epidote by Schmidt and Thompson (1996)
737 indicates that epidote can be stable up to790^{o}C and 10 kbar pressure but 50^{o}C lower at higher
738 pressures. Those authors also observed that minimum 5 kbar pressures required for magmatic
739 epidote to crystallize. Primary magmatic epidote found as euhedral crystals within hornblende
740 or poikilitically enclosed in hornblende indicates early crystallization epidote. Presence of
741 epidote stable in a granitic magma points to a minimum pressure of 5 kbar corresponding to ~
742 15 km depth. This conclusion is supported by the frequent presence of resorbed epidote, which
743 indicates its crystallization at the limit of its stability field. We can therefore conclude that 3.0
744 Ga Bellur-Nagamangala granite magmas crystallized at pressure close to 5 kbars(i.e., 15 km)

745 within the crust. However, magmatic epidote stability largely depends on temperature, pressure
746 and water activity.

747 In order to account for the above scenario, we consider the possibility of either spatial
748 link between the eruption of voluminous komatiite and komatiitic basalts in Nagamangala
749 greenstone belt (Tushipokla and Jayananda, 2013) or a link with an enriched mantle plume
750 emplaced beneath the crust. In the first scenario voluminous ~3.15 Ga komatiite to komatiite
751 basalt magmas might have caused heat advection and crust thickening through underplating as
752 well as thermal blanketing of the uppermost crust through eruption. The high thermal flux
753 initiated the melting of TTG basement, thus giving rise to the felsic end-member of the Bellur-
754 Nagamangala granites. As the generated melts began to crystallize, shrinkage cracks developed
755 to the mantle depth, causing low degree melting of the sub-continental mantle, which generated
756 the enriched mafic magmas that penetrated the crystallizing granite melts, thereby, causing
757 mixing and mingling. It is difficult to provide a satisfactory explanation for the large time gap
758 (ca. 150 Ma) between the 3.15 Ga greenstone volcanism and emplacement of ca. 3.0 Ga
759 granites. However, it should be noted that the uncertainty on the age for Banasandra komatiites
760 is also 150 My. Consequently, the time gap may well be shorter than currently assumed.
761 Alternatively, a 3.0 Ga mantle hotspot beneath the present exposure level of Bellur-
762 Nagamangala can be considered. Such mantle hotspot probably stalled at greater depth as
763 matured 3.3-3.15 Ga crust acted as thermal barrier. Continuous heating can cause low degree
764 melting of sub-continental mantle which generates enriched mafic to intermediate magmas.
765 These magmas upon their ascent into the lower crust can have induce partial melting of the
766 surrounding crust. Both magmas interact, mix and mingle during their emplacement at higher
767 levels as indicated by euhedral quartz/feldspars and magmatic epidote.

768

769 7.3 Origin of 2.6 Ga Pandavpura granite

We have petrographic, U-Pb and elemental data for only two samples. These rocks show similar elemental compositions to that of 2.61 Ga Arsikere-Banavara granites found further north which have been attributed to lower crustal melting (Jayananda et al., 2006). The high-REE concentrations together with moderate to poorly fractionated REE patterns with strong negative Eu anomalies indicate crustal source. Their high HREE contents coupled with poorly fractionated REE patterns preclude any role of garnet in the melt residue. The above arguments suggest an origin for the Pandavpura granites by reworking of lower crust.

7.4 Potassic granites as markers of crust-mantle interactions and cratonization in the WDC

As in almost all cratons (see, Laurent *et al.*, 2014; Moyen *et al.*, 2003) the potassic granites in the WDC correspond to the terminal event of crust genesis and craton building processes. They were partly generated by reworking of an older continental crust with minor mantle input. The TTGs in the western Dharwar craton formed 3600-3320 Ma ago, the last phase of TTGs emplaced at 3200 Ma. Immediately after, at 3150 Ma, sporadic transitional plutonic bodies were intruded, immediately followed at ca. 3080 Ma, by a high grade metamorphic event that is documented by texturally controlled in *situ*-monazite dating, discordant zircons with Pb-loss and metamorphic titanites (Banerjee et al., 2011; Jayananda et al., 2013, 2015).

The 3.2 Ga granodiorite intrusion is spatially associated with terminal event of crust formation in the WDC. It possibly marks a first stage of reworking as they contain inherited zircon dated at 3.3 Ga. The 3.0 Ga plutons emplacement was preceded by the eruption of komatiites and komatiitic-basalts in the adjoining Nagamangala belt and further north in the Banasandra belt at 3.15 Ga (Jayananda et al., 2008; Tushipokla and Jayananda, 2013; Maya et al., 2017). This suggests that ca. 3.0Ga potassic granite magmatism corresponds to a major tectonothermal event at the end of TTG accretion and greenstone volcanism. The ca. 3.0 Ga potassic magmatism marks the end of the juvenile crust accretion cycle and marks the first

795 stage of cratonization of Archean crust in the WDCn. The second stage of reworking consisted
796 in the emplacement of ca. 2.62 Ga potassic granites in Arsikere-Banavara and further north in
797 Hosdurga and Chitradurga region. The ca. 2.6 Ga Pandavpura potassic plutons forms the
798 southern extension of Chitradurga and Hosdurga granites and corresponds to very end of
799 cratonization. The ca. 2.56-2.52 Ga widespread juvenile magmatism of sanukitoid affinity
800 (Martin *et al.*, 2010) documented in in the central and eastern cratonic blocks (Moyen *et al.*,
801 1997; Jayananda et al., 1995, 2000, 2018; Moyen et al., 2001, 2003) is totally absent in the
802 WDC marking the distinct crustal evolution patterns in the cratonic blocks.
803
804 **8. Conclusions**
805 The conclusions of the present study can be summarized as follows:
806 1. The Bellur-Nagamangala-Pandavpura crustal corridor witness three main magmatic
807 events ca. 3.2 Ga, 3.0 Ga and 2.6 Ga.
808 2. The emplacement of 3.2 Ga granodiorite can correlated with 3.2 Ga diapiric
809 trondhjemites further west, which possibly corresponds to the end of juvenile crust
810 formation and first stage stabilization of the WDC.
811 3. Elemental and Nd isotope data in 3.0 Ga potassic granites suggest their origin by
812 melting of composite sources involving dominant TTG and minor enriched mantle.
813 4. Major and trace element data 2.6 Ga granites formed by crustal reworking of l TTG .
814 5. Magmatic epidote found in these granites points to their crystallization at about 5 kbars
815 prior to the emplacement at shallower levels.
816 **6.** Our new geochronological, elemental and Nd isotope data together with published data
817 show that the western Dharwar craton formed by successive stages of TTG-greenstone
818 accretion during 3.6-3.2 Ga and cratonized through reworking and intrusion of potassic
819 granites at 3.2 Ga, 3.0 Ga and 2.6 Ga.

Acknowledgments:

This work initially financed by IFCPAR project 1111-A and continued by UGC funded project (F-42-72/2013(SR) during 2013–2014). M.J acknowledge the support T. Kano (Yamaguchi University) for major and trace element analysis and D. Chardon for discussions on the geology of Dharwar craton over years. T.Tarun Thomas was financially supported by DST-INSPIRE Fellowship for his PhD program. We are grateful for constructive reviews by Roberto Dall'Agnol and Asko Kapyaho that helped to improve the quality of this contribution, together with the good editorial handling by Sukanta Dey.

Martin Guitreau acknowledges financial support from ClerVolc, the Université Clermont Auvergne, and the French Agence National de la Recherche through the funded research project *Zircontinents*. This manuscript is ClerVolc contribution 317. Jean-Marc Hénot and Jean-Luc Piro are thanked for technical assistance with CL imaging and LA-ICP-MS analyses at LMV. Jean-Louis Paquette is thanked for kindly providing good quality epoxy.

References:

Allègre, C.J. and Rousseau, D. (1984). The growth of the continents through geological time studied by Nd isotope analysis of shales. *Earth and Planetary Science Letters* **67**, 19-34.

Banerjee, M., Dasgupta, S., Pant, N.C., Jayananda, M. 2011. Contrasting metamorphic styles in the Dharwar craton. International Symposium on Precambrian accretionary orogens. Geological Society of India, Abstract volume. P 80.

Balakrishnan, S., Rajamani, V., Hanson, G.N., 1999. U–Pb ages for zircon and titani fromthe Ramagiri area, southern India: evidence for accretionary origin of the Eastern Dharwar craton during the late Archaean. J. Geol. 107, 69–86. http://dx.doi.

org/10.1086/314331.

844 Barbarin, B. and Didier, J., 1992. Genesis and evolution of mafic microgranular enclaves
845 through various types of interaction between coexisting felsic and mafic magmas. Earth and
846 Environmental Science Transactions of the Royal Society of Edinburgh, 83(1-2): 145-153.

847 Barker, F., 1979. Trondhjemite: definition, environment and hypothesis of origin. In: Barker,
848 F. (Ed.), Trondhjemites, Dacites and Related Rocks. Elsevier, Amsterdam, pp. 1–12.

849 Barker, F., Arth, J.G., 1976. Generation of trondhjemite-tonalite liquids and Archean bimodal
850 trondhjemite-basalt suites. Geology 4, 596–600.

851 Bhaskar Rao, Y.J., Griffin, W.L., Ketchum, J., Pearson, N.J., Beyer, E., O'Reilly, S.Y., 2008.
852 An outline of juvenile crust formation and recycling history in the Archaean Western Dharwar
853 craton, from zircon in situ U–Pb dating and Hf-isotopic compositions. Goldschmidt
854 Conference. Geochimica Cosmochimica Acta 72, A81.

855 Blundy, J. and Cashman, K., 2001. Ascent-driven crystallisation of dacite magmas at Mount
856 St Helens, 1980-1986. Contributions to Mineralogy and Petrology, 140(6): 631-650.

857 Bouhallier, H., Chardon, D. and Choukroune, P., 1995. Strain patterns in Archaean dome-and-
858 basin structures: the Dharwar craton (Karnataka, South India). Earth and Planetary Science
859 Letters 135, 57-75.

860 Bouhallier, H., Choukroune, P. and Ballèvre, M., 1993. Diapirism, bulk homogeneous
861 shortening and transcurrent shearing in the Archaean Dharwar craton: the Holenarsipur area,
862 southern India. Precambrian Research 63, 43-58.

863 Cawood, P.A., Hawkesworth, C.J. and Dhuime, B. (2013). The continental record and the
864 generation of continental crust. Geological Society of America Bulletin **125**, 14-32.

865 Chadwick, B., Vasudev, V.N., and Hedge, G.V., 2000. The Dharwar craton, southern India,
866 interpreted as the result of late Archaean oblique convergence: Precambrian Research, v. 99,
867 p. 91–101. doi:10.1016/S0301-9268(99) 00055-8.

868 Chadwick, B., Vasudev, V., Hegde, G.V., Nutman, A.P., 2007. Structure and SHRIMP U-Pb
869 zircon ages of granites adjacent to the Chitradurga schist belt: implications for Neoarchean
870 convergence in the Dharwar craton, southern India. Journal of the Geological Society of India
871 69, 5–24.

872 Chardon, D., Choukroune, P., Jayananda, M., 1996. Strain patterns, de´collement and incipient
873 sagducted greenstone terrains in the Archaean Dharwar craton (south India). Journal of
874 Structural Geology, 18, 991–1004.

875 Chardon, D., Choukroune, P., Jayananda, M., 1998. Sinking of the Dharwar basin (South
876 India): implications for Archaean tectonics. Precambrian Research 91, 15–39.

877 Chardon, D., Jayananda, M., Chetty, T.R.K., Peucat, J-J., 2008. Precambrian continental strain
878 and shear zone patterns: the South Indian case. Journal of Geophysical Research 113, B08402,
879 doi:10. 1029/ 2007JB005299.

880 Chardon, D., Jayananda, M., 2008. A 3D field perspective on deformation, flow and growth of
881 the lower continental crust. Tectonics 27, TC1014. http://dx.doi.org/ 10.1029/2007 TC002120.

882 Chardon, D., Jayananda, M., Peucat, J-J., 2011. Lateral constrictional flow of hot orogenic
883 crust: Insights from the Neoarchean of South India, geological and geophysical implications
884 for orogenic plateaux. Geochemistry Geophysics Geosystems 12, Q02005,
885 doi:10.1029/2010GC003398.

886 Choukroune, P., Bouhallier, H. and Arndt, N.T., 1994. Soft lithosphere during periods of
887 Archaean crustal growth or crustal reworking. In: M.P. Coward and A.C. Riess (Eds.), Early
888 Precambrian Processes. Geol, Soc, London, Spec, Publ., v.95, pp.67-86.

889 Corfu, F., 2003. Extraction of Pb with artificially too-old ages during stepwise dissolution
890 experiments on Archean zircon. Lithos 53, 279–291. Debon, F. and Le Fort, P., 1983. A
891 chemical-mineralogical classification of common plutonic rocks and associations.
892 Transactions of the Royal Society of Edinburgh Earth Sciences, 73: 135–149.
893 Deloule, E., Alexandrov, P., Cheilletz, A., Laumonier, B., 2002. Zircon U–Pb ion probe dating
894 of the gneisses and granites from the Canigou–Caranc¸a massif (eastern Pyr´en´ees, France):
895 irrelevance of the Cadomian basement/Paleozoic cover model. Int. J. Earth
896 Sci. 91, 398–405.
897 Devapriyan, G.V., Anantharamu, T.R., Vidyadharan, K.T., Raghu Nandan, K.R., 1994.
898 Spinifex textured peridotitic komatiite from Honnabetta area, Nagamangala
899 schist belt, Karnataka. Journal of Geological Society of India 44, 483-493.

900 Dey, S., 2013. Evolution of Archean crust in the Dharwar craton: the Nd isotope record.
901 Precambrian Res. 227, 227–246.

902 Dey, S., Pal, S., Balakristhe complete referencehnan, S., Halla, J., Kurhila, M., Heilimo,, E.
903 2018. Both plume and arc: origin of Neoarchaean crust as recorded in Veligallu greenstone belt
904 Dharwar craton, India, Precambrian Research. https://doi.org/10.1016/j.precamres.
905 2018.04.019
906 Dey, S., Pandey, U.K., Rai, A.K., Chaki, A., 2012. Geochemical and Nd isotope constraints
907 on petrogenesis of granitoids from NW part of the eastern Dharwar craton: possible
908 implications for late Archaean crustal accretion. Journal of Asian Earth Sciences 45, 40–
909 56.

910 Dhuime, B., Hawkesworth, C.J., Cawood, P.A. & Storey, C.D. 2012. A change in the
911 geodynamic of continental growth 3 billion years ago. Science, 335, 1334– 1336.

912 Goodwin, A.M. (1996). Principles of Precambrian Geology (Academic Press, 1996), pp. 327.

913 Gautier, N., Moyen, J-F, Stevens, G 2016. Diversity of burial rates in convergence settings
914 decreased as the Earth aged. Scientific Reports [6:26359] DOI: 10 1038/Srep26359

915 Guitreau, M., and Blichert-Toft, J., 2014. Implications of discordant U-Pb ages on Hf isotope
916 studies of detrital zircons. Chemical Geology 385, 17-25.

917 Guitreau, M., Mukusa, S.B., Loudin, L., Krishnan, S., 2017. New constraints on early
918 formation of western Dharwar craton (India) from igneous zircon U-Pb and Lu-Hf isotopes.
919 Precambrian Research, 302: 33-49.

920 Guitreau, M., Mora, N., & Paquette, J.-L. (2018). Crystallization and disturbance histories of
921 single zircon crystals from Hadean-Eoarchean Acasta gneisses examined by LA-ICP-MS U-
922 Pb traverses. Geochemistry, Geophysics, Geosystems, 19, 1-20.

923 Gupta, S., Rai, S.S., Prakasam, K.S., Srinagesh, D., Chadha, R.K., Priestley, P., Gaur, V.K.,
924 2003. First evidence for anomalous thick crust beneath mid-Archean western Dharwar craton.
925 Current Science 84, 1219–1225.

926 Hallot, E., Davy, P., de Bremond d'Ars, J., Auvray, B., Martin, H. and vanDamme, H., 1996.
927 Non-Newtonian effects during injection in partially crystallised magmas. Journal of Volcanic
928 and Geothermal Research, 71: 31-44.

929 Harish Kumar, S.B., Jayananda, M., Kano, T., Shadakshara Swamy, N., Mahabaleshwar, B.,
930 2003. Late Archean juvenile accretion process in the Eastern Dharwar Craton; Kuppam–
931 Karimangala area. Memoirs of the Geological Society of India 50, 375–408.

932 Heilimo, E., Halla, J., Holtta, P., 2010. Discrimination and origin of the sanukitoid series:

933 geochemical constraints from the Neoarchaean western Karelian Province (Finland).
934 Lithos 115, 27–39.

935 Iswar Kumar, C., Santosh, M., Wilde, S.A., Tsunogae, T., Itaya, T., Windley,B.F. Sajeev, K.,
936 2016 Mesoproterozoic suturing of Archean crustal blocks in western Peninsular India:
937 Implications for India-Madagascar correlations. Lithos, 263, 143-160.

938 Iizuka, T., Hirata, T., Komiya, T., Rino, S., Katayama, I., Motoki, A. and Maruyama, S. (2005).
939 U-Pb and Lu-Hf isotope systematics of zircons from the Mississippi river sand: implications
940 for reworking and growth of continental crust. *Geology* **33**, 485-488.

941 Janoušĕk, V., Moyen, J.-F., Martin, H., Erban, V. and Farrow, C., 2015. Geochemical
942 modelling of igneous processes-Principles and recipes in R Language. Bringing the power of
943 R to a wider community. Springer Geochemistry. Springer-Verlag, Berlin and Heidelberg, 346
944 pp.

945 Jayananda, M, Banerjee, M., Pant, N.C., Dasgupta, S., Kano, T., Mahesha, N., Mahableswar,
946 B. 2011. 2.62 Ga high-temperature metamorphism in the central part of the Eastern Dharwar
947 Craton: implications for late Achaean tectonothermal history. Geological
948 Journal 46: doi:10.1002/gj.1308.

949 Jayananda, M, Peucat, J-J., Chardon, D., Krishna Rao, B and Corfu, F., 2013a Neoarchean
950 greenstone volcanism, Dharwar craton, Southern India: Constraints from SIMS zircon
951 geochronology and Nd isotopes. Precambrian Research, 227, 55-76, doi.org/10.1016/
952 j.precamres.2012.05.002.

953 Jayananda, M., Tsutsumi,Y., Miyazaki, T., Gireesh, R.V., Kowe -u Kapfo, Tushipokla, Hidaka,
954 H., Kano., 2013b. Geochronological constraints on Meso-neoarchean regional metamorphism
955 and magmatism in the Dharwar craton, southern India. Journal of Asian Earth Sciences, 78,
956 18-38, doi.org/ 10.1016/j.jseaes. 2013.04.033.

957 Jayananda, M., Chardon, D., Peucat, -J.-J., and Fanning, C.M., 2015, Paleo- to Mesoarchean
958 TTG accretion and continental growth, western Dharwar craton, southern India: SHRIMP U-
959 Pb zircon geochronology, whole-rock geochemistry and Nd-Sr isotopes: Precambrian
960 Research, v. 268, p. 295–322. doi:10.1016/j.precamres.2015.07.015

961 Jayananda, M., Chardon, D., Peucat, J-J., Capdevila, R., 2006. 2.61 Ga potassic granites and
962 crustal reworking in the western Dharwar craton, southern India: Tectonic, geochronologic and
963 geochemical constraints. Precambrian Research 150, 1-26.

964 Jayananda, M., Kano, T., Peucat, J-J., Channabasappa, S., 2008. 3.35 Ga komatiite volcanism
965 in the western Dharwar craton: constraints from Nd isotopes and whole rock geochemistry.
966 Precambrian Research 162, 160-179. doi:10.1016/j.precamres. 2007.07.010 Elsevier.

967 Jayananda, M., Miyazaki, T., Gireesh, R.V., Mahesha, N., Kano, T., 2009. Synplutonic
968 mafic dykes from late Archaean granitoids in the Eastern Dharwar Craton southern
969 India. J. Geol. Soc. India 73, 117–130.

970 Jayananda, M., Martin, H., Peucat, J.-J. & Mahabaleswar, B. 1995. Late Archaean crust-mantle
971 interactions: geochemistry of LREE-enriched mantle derived magmas. Example of the
972 Closepet batholith, southern India. Contributions to Mineralogy and Petrology, 119, 314–329.

973 Jayananda, M., Moyen, J.F., Martin, H., Peucat, J.J., Auvray, B., Mahabaleswar, B. 2000. Late
974 Archean (2550-2520) juvenile magmatism in the Eastern Dharwar Craton, southern India:
975 constraints from geochronology, Nd–Sr isotopes and whole rock geochemistry. Precambrian
976 Research, 99, 225-254.

977 Jayananda, M., Gireesh, R.V., Sekhamo, Kowete-u, Miyazaki, T., 2014. Coeval Felsic and
978 Mafic Magmas in Neoarchean Calc-alkaline Magmatic Arcs, Dharwar Craton,Southern India:
979 Field and Petrographic Evidence from Mafic to Hybrid Magmatic Enclaves and Synplutonic
980 Mafic Dykes. J. Geol. Soc. India 84, 5–28.

981 Kamber, B.S., 2015. The evolving nature of terrestrial crust from the Hadean, through the
982 Archaean, into the Proterozoic. Precambrian Research 258, 48-82.

983 Khanna, T.C., Sesha Sai, V.V., Bizimis, M., Krishna, A.K., 2016. Petrogenesis of ultramafics
984 in the Neoarchean Veligallu greenstone terrane, eastern Dharwar craton,
985 India: constraints from bulk-rock geochemistry and Lu-Hf isotopes. Precambrian Res.
986 285, 186–201.

987 Laurent, O., Doucelance, R., Martin, H. and Moyen, J.-F., 2013. Differentiation of the late-
988 Archaean sanukitoid series and some implications for crustal growth: Insights from
989 geochemical modelling on the Bulai pluton, Central Limpopo Belt, South Africa. Precambrian
990 Research, 227(0): 186-203.

991 Laurent, O., Martin, H., Moyen, J.-F. and Doucelance, R., 2014. The diversity and evolution
992 of late-Archean granitoids: Evidence for the onset of "modern-style" plate tectonics between
993 3.0 and 2.5 Ga. Lithos, 205(0): 208-235.

994 Lancaster, P.J., Dey S., Storey, C.D., Mitra, A.M., Bhunia., R.K., 2015. Contrasting crustal
995 evolution processes in the Dharwar craton: Insights from detritalzircon U–Pb and Hf isotopes.

996 Ludwig, K.R., 2001. Users Manual for Isoplot/Ex rev. 2.49. A Geochronological Toolkit for
997 Microsoft Excel. Berkeley Geochronology Center Special Publication. No. 1a, 2455 Ridge
998 Road, Berkeley, CA 94709, USA.

999 Martin, H., 1986. Effect of steeper Archean geothermal gradient on geochemistry of
1000 subduction-zone magmas. Geology, 14: 753-756.

1001 Martin, H., 1993. The mechanisms of petrogenesis of the Archaean continental crust-
1002 comparison with modern processes. Lithos, 30: 373-388.

1003 Martin, H., 1999. The adakitic magmas: modern analogues of Archaean granitoids. Lithos,
1004 46(3): 411-429.

1005 Martin, H., Moyen, J.-F. and Rapp, R., 2010. The sanukitoid series: magmatism at the
1006 Archaean–Proterozoic transition Geological Society of America Special Papers, 472: 15-33.

1007 Martin, H., Smithies, R.H., Rapp, R., Moyen, J.-F. and Champion, D., 2005. An overview of
1008 adakite, tonalite-trondhjemite-granodiorite (TTG), and sanukitoid: relationships and some
1009 implications for crustal evolution. Lithos, 79(1-2): 1-24.

1010 Maya, J.M., Bhutani, R., Balakrishnan, S., and Rajee Sandhya, S., 2017. Petrogenesis of 3.15
1011 Ga old Banasandra komatiites from the Dharwar craton, India: Implications for early mantle
1012 heterogeneity. Geoscience Frontiers 8, 467-481.

1013 Meen, J.K., Rogers, J.J.W., Fullagar, P.D., 1992. Lead isotopic compositions in the western
1014 Dharwar craton, southern India: evidence for distinct middle Archaean terrains in a late
1015 Archaean craton. Geochimica et Cosmochimica Acta 56, 2455–2470.

1016 Mohan, M.R., Sarma, D.S., Mc Naughton, N.J., Fletcher, I.R., Wilde, S.A., Siddiqui, M.H.,

1017 Rasmussen, B., Krapez, B., Gregory, C.J., Kamo, S.L., 2014. SHRIMP zircon and titanite U-
1018 Pb ages, Lu-Hf isotope signatures and geochemical constraints for 2.56 Gabgranite magmatism
1019 in western Dharwar craton, southern India: evidence for shortlived Neoarchean episodic crustal
1020 growth. Precambrian Res. 243, 197–220.

1021 Moyen, J.-F. and Martin, H., 2012. Forty years of TTG research. Lithos, 148: 312-336.

1022 Moyen, J.-F., Martin, H. and Jayananda, M., 1997. Origine du granite fini-Archéen de Closepet
1023 (Inde du Sud): apports de la modélisation géochimique du comportement des éléments en
1024 traces. Compte Rendus de l'Académie des Sciences de Paris, 325: 659-664.

1025 Moyen, J.-F., Martin, H. and Jayananda, M., 2001. Multi-element geochemical modelling of
1026 crust-mantle interactions during late-Archaean crustal growth : the Closepet granite (South
1027 India). Precambrian Research, 112: 87-105.

1028 Moyen, J.-F., Martin, H., Jayananda, M. and Auvray, B., 2003. Late Archaean granites: a
1029 typology based on the Dharwar Craton (India). Precambrian Research, 127(1-3): 103-123.

1030 O'Connor, J.T., 1965. A classification for quartz-rich igneous rocks based on feldspar ratios.
1031 In: U.S. Geological Survey Professionnal Paper 525 (B)., pp. 79–84.

1032 Nutman, A.P., Chadwick, B., Krishna Rao, B., Vasudev, V.N., 1996. SHRIMP U/Pb zircon
1033 ages of acid volcanic rocks in the Chitradurga and Sandur groups, and granites adjacent
1034 to the Sandur Schist belt, Karnataka. J. Geol. Soc. India 47, 153–164.

1035 Paces, J.B., Miller Jr, J.D., 1993. Precise U-Pb ages of Duluth Complex and related mafic
1036 intrusions, Northeastern Minnesota: geochronological insights to physical, petrogenetic,
1037 paleomagnetic, and tectonomagmatic processes associated with the 1.1 GaMidcontinent Rift
1038 System. J. Geophys. Res. 98, 13997–14013.

1039 Peucat, J.-J., Mahabaleswar, M., Jayananda, M., 1993. Age of younger tonalitic magmatism
1040 and granulite metamorphism in the amphibolite–granulite transition zone of southern India
1041 (Krishnagiri area): comparison with older Peninsular gneisses of Gorur- Hassan area. Journal
1042 of Metamorphic Geology 11, 879–888.

1043 Peucat, J-J., Bouhallier, H., Fanning, C.M., Jayananda, M., 1995. Age of Holenarsipur schist
1044 belt, relationships with the surrounding gneisses (Karnataka, south India). Journal of Geology
1045 103, 701-710.

1046 Peucat, J-J., Jayananda, M. Chardon, D., Capdevila, R., Fanning Marc. C., Paquette, J-L., 2013.
1047 The lower crust of Dharwar craton, south India: Patchwork of Archean granulitic domains.
1048 Precambrian Research, 227, 4-29 http://dx.doi.org/10.1016/ j.precamres.2012.06.009.

1049 Raase, P., Raith, M., Ackermand, D., Lal, R.K. 1986. Progressive metamorphism of mafic
1050 rocks from greenschist to granulite facies in the Dharwar craton of South India. Journal of
1051 Geology 94, 261–282.

1052 Ramakrishnan, M., Viswanatha, M.N., Swami Nath, J., 1976. Basement-cover relationships of
1053 Peninsular Gneisses with high grade schists and greenstone belts of southern Karnataka. J.
1054 Geol. Soc. India 17, 97-111.

1055 Roberts, N.M.W., Spencer, C.J. (2014) The zircon archive of continent formation through
1056 time. Geological Society of London Special Publications 389, 197-225.

1057 Rogers, J. J. W. and Callahan, E . J., 1989. Diapiric trondhjemites of the Western Dharwar
1058 craton, southern India. Canadian Journal of Earth Sciences, 26, 244-256.

1059 Satyanarayanan, M., Balaram, V., Sawant, S. S., Subramanyam, K. S. V., Vamsi Krishna, G.,
1060 Dasaram, B., & Manikyamba, C. (2018). Rapid determination of REE, PGE, and other trace
1061 elements in geological and environmental materials by high resolution inductively coupled
1062 plasma mass spectrometry. Atomic Spectroscopy, 39(1), 1–15.

1063
1064 Shand, S.J., 1943. Eruptive rocks. Their genesis, composition, classification and their relations
1065 to ore-deposits., New York, 444 pp.

1066 Sláma, J., J. Košler, D.J. Condon, J.L. Crowley, A. Gerdes, J.M. Hanchar, M.S.A. Horstwood,
1067 G.A. Morris, L. Nasdala, N. Norberg, U. Schaltegger, B. Schoene, M.N. Tubrett, and M.J.
1068 Whitehouse (2008), Plesovice zircon -- A new natural reference material for U-Pb and Hf
1069 isotopic microanalysis. Chem. Geol. 249, 1-35.

1070 Streckeisen, A., Le Maitre, R.W., 1979. A chemical approximation to the modal QAPF
1071 classification of the igneous rocks. N. Jahrb.Mineral. Abt. 136, 169–206.

1072 Swami Nath, J., Ramakrishnan, M., Viswanatha, M.N., 1976. Dharwar stratigraphic

model and Karnataka craton evolution. Rec. Geol. Surv. India 107, 149–175.

Swami Nath, J., Ramakrishnan, M. (Eds.), 1981. Early Precambrian Supracrustals of Southern Karnataka. Geological Survey of India, Memoir 112, p. 350.

Taylor, S.R. and McLennan, S.M. (1985). The continental crust: its composition and evolution. Blackwell Scientific Publications.

Tushipokla., Jayananda, M., 2013. Geochemical constraints on komatiite volcanism from Sargur Group Nagamangala greenstone belt, western Dharwar craton, southern India: Implications for Mesoarchean mantle evolution and continental growth. Geoscience Frontiers, 4, 321-340.

Tuttle, O.F. and Bowen, N.L., 1958. Origin of granite in the light of experimental studies in the system $NaAlSi_3O_8$-$KAlSi_3O_8$-SiO_2-H_2O. The Geological Society of America Memoir, 74.

Valley, J.W., Lackey, J.S., Cavose, A.J., Clenchencko, C.C. Spicuzza, M.J., Basei, M.A.S., Bindeman, I.N., Ferreira, V.P., Sial, A.N., King, E.M., Peck, W.H., Peck, W.H., Sinha, A.K., Wei, C.S.S. 2005. 4.4 billion years of crustal maturation :Oxygen isotope ratios of magmatic rocks. Contributions to Mineralogy and Petrology, 150, 561-580.

Wiedenbeck, M., Hanchar, J.M., Peck, W.H., Sylvester, P., Valley, J., Whitehouse, M., Kronz, A., Morishita, Y., Nasdala, L., Fiebig, J., Franchi, I., Girard, J.P., Greenwood, R.C., Hinton, R., Kita, N., Mason, P.R.D., Norman, M., Ogasawara, M., Piccoli, R., Rhede, D., Satoh, H., Schulz-Dobrick, B., Skår, O., Spicuzza, M.J., Terada, K., Tindle, A., Togashi, S., Vennemann, T., Xie, Q., Zheng, Y.-F., 2004. Further characterization of the 91500 zircon crystal. Geostand. Geoanal. Res. 28, 9–39.

Captions to figures and tables

Figure 1. Geological sketch map of the Dharwar craton (modified after Geological Survey of India, project Vasundeara)

Figure 2. Geological sketch map of the Bellur-Nagamangala region (Western Dharwar craton) modified after Geological Survey of India resource map (Mandya district, 2000).

Figure 3. Field photographs illustrating the outcropping conditions of the studied granites

Figure 4. Optical microscope images of thin section made on granites… showing the presence of euhedral epidote both as inclusions in biotite and hornblende, and as matrix minerals.

Figure 5. U-Pb concordia plot for the zircon crystals analyzed by SIMS and LA-ICP-MS. BSE and transmitted light images of some of the analyzed grains are also provided. See text for details.

Figure 6. (A) Normative An-Ab-Or diagram (Barker, 1979; O'Connor, 1965), showing that almost all of Bellur samples fall in the granite field. Their composition is very different from that of Archaean TTG. (B) Streckeisen and Le Maitre (1979) Q'- ANOR diagram showing the two parallel plutonic trends for the studied plutons. The fields are: To = tonalite; Tdh = trondhjemite; Gd = granodiorite; Gr = granite and CA = calc-alkaline trend (Barker and Arth, 1976).

Figure 7. (A) A/NK *vs.* A/CNK molar diagram (Shand, 1943), where A/NK = $Al_2O_3/(Na_2O+K_2O)$ and A/CNK = $Al_2O_3/(CaO+Na2O+K_2O)$ showing the metaluminous character of the Bellur granite;

Figure 8. CIPW normative Q-Ab-Or triangle (Blundy and Cashman, 2001), showing that the Bellur-Nagamangala granites plot near the minimum melt point of the 'hydrous granitic system' for pressures ranging between 2 and 10 kbar.

Figure 9. Harker's diagrams for major elements in the Bellur granites.

Figure 10. Harker's diagrams for trace elements in the Bellur granites.

Figure 11. (a-e) Chondrite normalized REE patterns, (f) $(La/Yb)_N$ *vs*. Yb_N diagram showing that the Bellur granites do not have any affinity for Archaean TTG compositions (orange field) but rather for modern calc-alkaline magmas (green field); (Martin, 1986) and (g-k) primitive mantle normalized multi-element diagram for the studied plutons. Shaded area in the REE and Spider diagram represents TTGs of the studied corridor.

Figure 12. (A) $^{147}Sm/^{144}Nd$ vs. $^{143}Nd/^{144}Nd$ plot showing a positive correlation which translates into an age of 2953 ± 225 Ma (2σ), or 2977 ± 115 Ma, when black-filled circles are excluded. (B) $^{143}Nd/^{144}Nd$ and εNd calculated at 3.0 Ga as a function of SiO_2 concentration showing a broad negative correlation for the studied granites. See text for details.

Fig. 13. 1/Er – (Ba+Sr)/1000 – Er triangular plot (Heilimo et al., 2010) depicting absence of garnet in melt residue of the source.

Table 1. LA-ICP-MS operating conditions

Table 2. Results for zircon U-Pb analysis by SIMS

Table 3. Results for zircon U-Pb analysis by LA-ICP-MS

Table 4. Major and trace element results for the studied granites

Table 5. Results for whole-rock Sm-Nd isotope measurements by TIMS

Table 1: LA-ICP-MS operating conditions

Analysis	*U-Pb geochronology*
Laboratory	Université Clermont Auvergne
ICP-MS model	Thermo Element XR
Forward Power	1300 W
Auxiliary gas (Ar)	~1.0 l/min
Ar sample	~0.7 l/min
Oxide ThO/Th	~0.5-1.5%
Additional gas	N2
Additional gas flow	7.0 ml/min
SQUID	On
Laser model	Resonetics Resolution M-50
Wavelength	193 nm
Pulse duration	<4 ns
Energy	~2.8 mJ
Fluence	2.5-2.6 J/cm2
Frequency	4 Hz
Spot size	33 µm
Carrier gas	He
Carrier gas flow	~0.7 l/min
Data acquisition	
Protocol	Time resolved analysis
Scanning mode	Peak-jumping
Dwell time per isotope	5 ms
Settling time	20 µs
Background counting time	20 s
Sample measurement time	60 s
Measurement type	Standard bracketing
External standard	91500, AS3, Plešovice
Masses measured	204, 206, 207, 208, 232, 238

Table 2: Results for zircon U-Pb analysis by SIMS

Grain. spot	U (ppm)	Th (ppm)	Pb* (ppm)	Th/U	Isotopic ratios $^{204}Pb/^{206}Pb$	f_{206} %	$^{206}Pb/^{238}U$	±	$^{207}Pb/^{235}U$	±	$^{207}Pb/^{206}Pb$
Zircon CHT2*: deformed porphyroide granite in the Chitradurga SZ (Nelligere, W. Kunigal) (L tecto											
1.1	426	569	213	1.34	0.000003	0.000	0.580	0.015	17.74	0.47	0.2214
2.1	453	234	132	0.52	0.000011	0.001	0.339	0.010	10.13	0.29	0.2163
2.2	270	161	93	0.60	0.000082	0.008	0.399	0.010	12.01	0.29	0.2189
3.1	746	530	261	0.71	0.000037	0.004	0.407	0.024	11.62	0.68	0.2072
4.1	225	187	107	0.83	0.000006	0.001	0.552	0.008	16.98	0.26	0.2230
5.1	114	98	59	0.86	0.000018	0.002	0.595	0.012	18.14	0.36	0.2209
Zircon BH50*: undeformed porhyroïde granite, W of the Chitradurga SZ (Nelligere, W. Kunigal)											
1.1	57	46	32	0.80	0.000029	0.003	0.654	0.008	23.16	0.30	0.2565
2.1	57	22	30	0.38	0.000022	0.002	0.619	0.010	20.81	0.34	0.2435
3.1	118	101	57	0.85	0.000027	0.003	0.559	0.011	16.96	0.34	0.2198
4.1	98	176	39	1.79	0.000037	0.004	0.458	0.023	14.07	0.71	0.2226
5.1	399	225	212	0.56	0.000006	0.001	0.619	0.008	21.80	0.28	0.2553
6.1	139	68	54	0.49	0.000083	0.008	0.451	0.006	13.65	0.18	0.2200
7.1	44	51	21	1.16	0.000026	0.003	0.568	0.007	17.23	0.23	0.2193
8.1	280	65	121	0.23	0.000124	0.012	0.504	0.011	16.22	0.37	0.2344
9.1	322	198	173	0.61	0.000144	0.014	0.625	0.012	21.79	0.44	0.2541
10.1	328	134	168	0.41	0.000007	0.001	0.597	0.011	21.01	0.37	0.2552

		Ages (in Ma)						
		$^{206}Pb/$		$^{207}Pb/$		$^{207}Pb/$		Conc.
±	r	^{238}U	±	^{235}U	±	^{206}Pb	±	%
nite, horizontal lineation)								
0.0008	0.99	2951	62	2975	25	2992	6	99
0.0003	1.00	1884	46	2446	26	2954	2	64
0.0003	1.00	2166	45	2606	23	2967	2	73
0.0011	1.00	2202	108	2574	53	2882	8	76
0.0005	0.99	2833	35	2934	15	3004	4	94
0.0006	0.99	3012	47	2997	19	2987	4	101
0.0005	0.99	3242	33	3234	13	3228	3	100
0.0012	0.95	3105	38	3130	16	3146	8	99
0.0007	0.99	2862	45	2932	19	2981	5	96
0.0010	1.00	2429	101	2754	47	3002	7	81
0.0003	0.99	3105	31	3175	12	3220	2	96
0.0004	0.99	2398	26	2726	12	2978	3	81
0.0004	0.99	2900	31	2948	13	2981	3	97
0.0008	0.98	2632	48	2890	22	3075	6	86
0.0006	0.99	3130	49	3174	19	3202	4	98
0.0002	1.00	3016	43	3139	17	3218	1	94

Table 3: Results for zircon U-Pb analysis by LA-ICP-MS

	Isotopic ratios							Age (Ma)			
Name	Pb207/U235	2σ	Pb206/U238	2σ	Rho	Pb207/Pb206	2σ	Pb207/U235	2σ	Pb206/U238	2σ
PAN-01											
PAN-01_1b	12.22	0.24	0.505	0.010	0.97	0.1755	0.0018	2622	18	2635	41
PAN-01_2	10.93	0.23	0.452	0.009	0.91	0.1754	0.0020	2517	20	2403	39
PAN-01_8a	11.97	0.23	0.497	0.009	0.96	0.1747	0.0018	2602	18	2601	40
PAN-01_8b	11.90	0.23	0.496	0.009	0.96	0.1740	0.0018	2596	19	2596	40
PAN-01_8c	11.81	0.23	0.494	0.009	0.97	0.1733	0.0018	2589	18	2589	40
PAN-01_8d	11.86	0.23	0.495	0.009	0.97	0.1736	0.0018	2593	18	2594	40
PAN-01_10a	12.06	0.24	0.499	0.009	0.96	0.1753	0.0018	2609	19	2609	41
PAN-01_10b	10.92	0.21	0.466	0.009	0.97	0.1700	0.0018	2516	18	2466	39
PAN-01_11c	11.33	0.24	0.469	0.009	0.96	0.1752	0.0018	2551	18	2479	41
PAN-01_13a	12.39	0.25	0.515	0.010	0.94	0.1744	0.0019	2635	19	2680	41
PAN-01_13b	11.77	0.24	0.487	0.009	0.96	0.1753	0.0019	2586	19	2557	41
PAN-01_14a	11.75	0.23	0.487	0.009	0.96	0.1751	0.0018	2585	18	2557	40
PAN-01_15	11.31	0.23	0.475	0.009	0.95	0.1724	0.0018	2549	19	2508	39
PAN-01_16c	11.94	0.24	0.496	0.009	0.94	0.1744	0.0019	2599	19	2598	41
PAN-01_19	11.98	0.24	0.497	0.009	0.94	0.1747	0.0019	2603	19	2602	40
PAN-01_20	11.95	0.24	0.496	0.009	0.94	0.1746	0.0019	2600	19	2597	40
PAN-01_28a	11.55	0.24	0.475	0.009	0.93	0.1765	0.0019	2569	19	2505	39
PAN-01_28b	11.78	0.23	0.494	0.009	0.95	0.1731	0.0018	2587	19	2587	40
PAN-01_33a	11.45	0.23	0.465	0.009	0.93	0.1788	0.0019	2561	19	2460	39
PAN-01_33b	11.85	0.24	0.495	0.009	0.94	0.1736	0.0019	2593	19	2593	40
PAN-01_35	12.10	0.24	0.508	0.010	0.94	0.1725	0.0018	2612	19	2650	41
PAN-01_36a	11.75	0.24	0.489	0.009	0.93	0.1743	0.0019	2584	19	2565	40
PAN-01_36b	12.02	0.24	0.498	0.009	0.93	0.1750	0.0019	2606	19	2606	40
PAN-02											
PAN-02_1	12.10	0.24	0.501	0.010	0.96	0.1750	0.0018	2612	19	2620	41
PAN-02_2	12.01	0.23	0.500	0.009	0.97	0.1741	0.0018	2605	18	2614	41
PAN-02_7	11.77	0.23	0.490	0.009	0.97	0.1740	0.0018	2586	18	2573	40
PAN-02_8	12.18	0.25	0.504	0.010	0.94	0.1752	0.0019	2618	19	2632	42
PAN-02_14	11.93	0.23	0.496	0.009	0.97	0.1744	0.0018	2599	18	2597	41
PAN-02_17a	11.62	0.23	0.482	0.009	0.96	0.1750	0.0018	2575	19	2535	40
PAN-02_18	12.16	0.24	0.506	0.010	0.97	0.1745	0.0018	2617	18	2638	41
PAN-02_19	12.42	0.24	0.512	0.010	0.97	0.1760	0.0018	2637	18	2664	41
PAN-02_20a	12.02	0.24	0.502	0.010	0.96	0.1737	0.0018	2606	19	2621	41
PAN-02_20b	12.16	0.24	0.509	0.010	0.97	0.1732	0.0018	2618	18	2653	41
PAN-02_21	12.12	0.24	0.500	0.009	0.97	0.1758	0.0018	2614	18	2613	41
PAN-02_23a	12.04	0.24	0.507	0.010	0.97	0.1723	0.0018	2607	18	2642	42
PAN-02_23b	12.01	0.24	0.502	0.010	0.97	0.1735	0.0018	2606	19	2623	41
PAN-02_24	12.11	0.24	0.499	0.009	0.96	0.1758	0.0018	2613	19	2611	41
PAN-02_26a	12.15	0.25	0.504	0.010	0.93	0.1747	0.0019	2616	19	2633	41
PAN-02_26b	12.17	0.25	0.502	0.010	0.95	0.1758	0.0019	2617	19	2622	41
PAN-02_27b	11.81	0.24	0.489	0.009	0.94	0.1752	0.0019	2589	19	2566	40
5-J-5											
5-J-5_3	8.65	0.17	0.298	0.006	0.94	0.2103	0.0022	2302	18	1683	28
5-J-5_7	9.68	0.19	0.310	0.006	0.94	0.2264	0.0024	2404	19	1740	29
5-J-5_15	17.16	0.35	0.568	0.011	0.93	0.2191	0.0024	2944	20	2899	44
5-J-5_19	14.25	0.29	0.473	0.009	0.94	0.2187	0.0024	2767	19	2495	39
5-T48b											
5-T48b_3	14.44	0.28	0.476	0.009	0.96	0.2198	0.0023	2779	19	2511	39
5-T48b_7	17.98	0.36	0.592	0.011	0.95	0.2204	0.0023	2989	19	2996	45
5-T48b_8a	17.95	0.36	0.592	0.011	0.95	0.2199	0.0023	2987	19	2998	45

5-T48b_8b	12.33	0.24	0.390	0.007	0.95	0.2294	0.0024	2630	19	2122	34
5-T48b_12	9.31	0.18	0.288	0.005	0.95	0.2343	0.0025	2369	18	1633	27
5-T48b_13	12.61	0.27	0.408	0.008	0.91	0.2241	0.0025	2651	20	2206	36
5-T48b_16a	17.88	0.35	0.589	0.011	0.94	0.2203	0.0024	2983	19	2984	45
5-T48b_16b	17.95	0.36	0.590	0.011	0.94	0.2207	0.0024	2987	19	2988	46
5-T48b_28	7.56	0.15	0.237	0.005	0.93	0.2312	0.0025	2180	19	1371	23
NM-04											
NM-04_1	21.72	0.42	0.628	0.012	0.97	0.2507	0.0026	3171	19	3143	47
NM-04_4	22.69	0.45	0.647	0.013	0.97	0.2541	0.0026	3214	19	3218	49
NM-04_6	22.17	0.43	0.634	0.012	0.97	0.2534	0.0026	3191	19	3167	47
NM-04_10	15.45	0.33	0.449	0.009	0.91	0.2498	0.0029	2844	21	2390	39
NM-04_11	22.62	0.44	0.647	0.012	0.97	0.2534	0.0026	3211	19	3218	48
NM-04_12	22.37	0.43	0.640	0.012	0.97	0.2535	0.0026	3200	19	3189	47
MS-05											
MS-05_1a	23.09	0.45	0.623	0.012	0.97	0.2687	0.0028	3231	19	3123	47
MS-05_1b	12.18	0.24	0.343	0.006	0.97	0.2576	0.0027	2618	18	1900	31
MS-05_3	22.12	0.46	0.574	0.011	0.94	0.2795	0.0031	3189	20	2924	46
MS-05_4a	17.79	0.34	0.520	0.010	0.97	0.2479	0.0026	2979	19	2701	42
MS-05_4b	21.34	0.41	0.622	0.011	0.97	0.2490	0.0026	3154	19	3116	46
MS-05_5a	22.79	0.45	0.651	0.012	0.95	0.2539	0.0027	3218	20	3231	48
MS-05_5b	22.65	0.45	0.647	0.012	0.95	0.2537	0.0027	3212	20	3218	48
MS-05_6	23.26	0.45	0.653	0.012	0.96	0.2582	0.0027	3238	19	3240	48
MS-05_8a	25.09	0.49	0.672	0.013	0.96	0.2706	0.0028	3312	19	3314	49
MS-05_8b	25.07	0.49	0.672	0.013	0.96	0.2704	0.0028	3311	19	3314	49
MS-05_11	12.27	0.24	0.355	0.007	0.96	0.2505	0.0026	2625	18	1960	32
MS-05_12	18.51	0.36	0.501	0.009	0.96	0.2680	0.0028	3017	19	2618	41
Zircon standards											
AS3											
AS3_1	1.93	0.04	0.184	0.003	0.93	0.0761	0.0008	1092	14	1090	19
AS3_2	1.91	0.04	0.183	0.003	0.95	0.0756	0.0008	1084	13	1084	19
AS3_3	1.92	0.04	0.184	0.003	0.95	0.0758	0.0008	1088	13	1087	19
AS3_4	1.95	0.04	0.186	0.004	0.92	0.0757	0.0008	1097	14	1101	19
AS3_5	1.93	0.04	0.184	0.003	0.94	0.0759	0.0008	1091	13	1090	19
AS3_6	1.95	0.04	0.186	0.004	0.88	0.0758	0.0009	1097	15	1100	20
AS3_7	1.95	0.04	0.186	0.004	0.91	0.0761	0.0008	1100	14	1101	19
AS3_8	1.93	0.04	0.185	0.004	0.96	0.0758	0.0008	1092	13	1093	19
AS3_9	1.94	0.04	0.185	0.004	0.94	0.0759	0.0008	1095	14	1096	19
AS3_10	1.90	0.04	0.182	0.003	0.95	0.0756	0.0008	1082	13	1080	19
AS3_11	1.94	0.04	0.185	0.004	0.91	0.0758	0.0008	1094	14	1096	19
AS3_12	1.91	0.04	0.183	0.003	0.92	0.0759	0.0008	1085	14	1082	19
AS3_13	1.94	0.04	0.185	0.004	0.92	0.0759	0.0008	1095	14	1096	19
AS3_14	1.94	0.04	0.184	0.003	0.91	0.0763	0.0008	1094	14	1090	19
AS3_15	1.94	0.04	0.186	0.004	0.93	0.0758	0.0008	1096	14	1099	19
Plesovice											
Plesovice_1	0.38	0.01	0.051	0.001	0.91	0.0533	0.0006	324	7	322	8
Plesovice_2	0.37	0.01	0.051	0.001	0.94	0.0526	0.0006	321	7	323	8
Plesovice_3	0.38	0.01	0.051	0.001	0.92	0.0530	0.0006	324	8	323	8
Plesovice_4	0.37	0.01	0.051	0.001	0.92	0.0532	0.0006	322	7	320	8
Plesovice_5	0.39	0.01	0.054	0.001	0.90	0.0533	0.0006	338	8	337	8
Plesovice_6	0.40	0.01	0.054	0.001	0.91	0.0536	0.0006	340	8	337	8
Plesovice_7	0.37	0.01	0.051	0.001	0.90	0.0529	0.0006	323	7	323	8
Plesovice_8	0.37	0.01	0.051	0.001	0.95	0.0529	0.0006	323	7	323	8
Plesovice_9	0.39	0.01	0.053	0.001	0.94	0.0530	0.0006	334	7	334	8
Plesovice_10	0.38	0.01	0.052	0.001	0.93	0.0532	0.0006	328	7	326	8

Plesovice_11	0.39	0.01	0.053	0.001	0.86	0.0532	0.0006	334	8	334	8
Plesovice_12	0.39	0.01	0.053	0.001	0.86	0.0534	0.0006	334	8	333	8
Plesovice_13	0.39	0.01	0.052	0.001	0.90	0.0534	0.0006	332	8	330	8

)			Concentration (ppm)				
Pb207/Pb206	2σ	Disc.	206Pb/204Pb	Pb	Th	U	Th/U
2611	17	-1.2%	4080	70	64	95	0.67
2610	18	9.5%	5490	64	69	97	0.71
2603	17	0.1%	3430	49	50	68	0.74
2597	17	0.0%	12278	91	118	121	0.97
2589	17	0.0%	12998	106	113	147	0.77
2592	17	-0.1%	89111	115	122	157	0.78
2609	17	0.0%	3118	48	42	66	0.63
2558	17	4.3%	24507	227	170	351	0.48
2608	17	5.9%	2902	174	162	237	0.68
2600	18	-3.8%	836	29	35	37	0.94
2609	17	2.4%	1879	101	104	134	0.78
2607	17	2.3%	3837	172	225	230	0.98
2581	18	3.4%	3460	89	97	126	0.77
2600	18	0.1%	5646	51	50	72	0.70
2603	18	0.0%	3473	79	86	108	0.80
2603	18	0.3%	28532	58	57	80	0.70
2620	18	5.3%	7677	28	32	39	0.83
2587	18	0.0%	36124	142	127	202	0.63
2641	18	8.3%	2602	41	45	56	0.80
2593	18	0.0%	8536	161	138	226	0.61
2582	18	-3.2%	451450	111	99	153	0.65
2599	18	1.6%	6252	135	128	192	0.67
2606	18	0.0%	18776	96	98	131	0.75
2606	17	-0.7%	7081	32	39	43	0.91
2598	17	-0.8%	7978	58	60	79	0.76
2597	17	1.1%	5186	163	182	223	0.81
2608	18	-1.1%	2239	15	16	19	0.83
2600	17	0.1%	7193	64	68	88	0.78
2606	17	3.3%	1786	37	54	49	1.09
2601	17	-1.7%	7360	74	77	99	0.78
2616	17	-2.3%	3876	80	39	116	0.33
2594	17	-1.3%	5878	60	56	84	0.66
2589	17	-3.0%	17689	79	73	109	0.67
2614	17	0.0%	3533	98	73	140	0.52
2580	17	-3.0%	10718	211	178	288	0.62
2592	17	-1.5%	14667	90	98	120	0.82
2614	17	0.1%	3621	129	132	175	0.76
2603	18	-1.4%	3946	15	21	20	1.04
2614	17	-0.4%	5589	50	45	69	0.65
2608	18	2.0%	2971	80	69	115	0.60
2908	17	47.6%	520	201	388	408	0.95
3027	17	48.3%	869	242	312	469	0.67
2974	17	3.1%	2187	63	65	70	0.93
2971	17	19.3%	2175	332	280	466	0.60
2980	17	18.9%	1633	234	203	325	0.62
2984	17	-0.5%	10891	61	67	64	1.04
2980	17	-0.8%	17581	44	39	49	0.79

3048	17	35.5%	911	62	60	101	0.60
3082	17	53.0%	583	85	93	179	0.52
3011	18	31.4%	910	57	82	88	0.93
2983	17	2.1%	13643	78	88	84	1.05
2986	17	-1.7%	6863	64	64	69	0.94
3060	17	61.0%	561	94	204	223	0.91
3189	16	1.8%	7557	162	95	171	0.56
3211	16	-5.1%	8611	124	48	128	0.37
3206	16	1.5%	16888	69	22	77	0.29
3183	18	29.7%	128	6	1	9	0.14
3206	16	-0.5%	4644	148	84	152	0.55
3206	16	0.7%	6664	130	90	133	0.68
3299	16	5.1%	525710	149	87	157	0.55
3232	16	47.3%	1740	108	70	209	0.33
3360	17	16.1%	276	9	0	10	0.04
3172	16	18.1%	14996	156	80	207	0.39
3179	16	4.2%	486859	133	60	151	0.40
3209	17	-0.9%	3907	19	10	20	0.50
3208	17	-0.4%	64477	18	9	19	0.50
3236	16	-0.2%	7120	93	60	95	0.64
3310	16	-0.2%	16444	70	38	69	0.54
3309	16	-0.2%	9103	56	26	56	0.46
3188	16	44.5%	3623	95	68	179	0.38
3294	16	24.9%	9963	95	33	135	0.25
1096	21	0.6%	13939	49	124	199	0.62
1085	21	0.1%	10742	60	157	246	0.64
1091	21	0.4%	14254	59	156	237	0.66
1088	22	-1.3%	10408	54	138	215	0.64
1092	21	0.2%	15983	57	150	230	0.65
1091	23	-0.9%	6491	29	51	119	0.43
1097	22	-0.3%	12076	60	157	241	0.65
1091	21	-0.2%	355391	62	157	255	0.62
1092	21	-0.5%	7273	72	185	291	0.64
1086	21	0.6%	7440	84	217	346	0.63
1091	22	-0.5%	13981	53	153	210	0.73
1092	22	1.0%	18444	90	218	370	0.59
1092	22	-0.4%	7651	83	233	327	0.71
1102	22	1.3%	4880	62	165	253	0.65
1090	21	-0.9%	8923	76	196	303	0.65
343	24	6.2%	8566	32	47	549	0.09
313	24	-3.0%	3935	34	52	586	0.09
327	25	1.4%	187239	38	60	654	0.09
338	24	5.4%	181680	37	56	643	0.09
341	25	1.0%	4002	34	49	574	0.09
355	25	5.1%	14347	37	58	639	0.09
323	25	0.1%	6839	35	53	605	0.09
325	24	0.6%	4195	35	52	594	0.09
330	24	-1.2%	13970	41	64	677	0.10
336	24	3.0%	245476	39	61	664	0.09

337	26	1.0%	143963	24	33	394	0.08
346	26	3.8%	1752	21	28	357	0.08
346	25	4.7%	9234	40	60	666	0.09

Table 4. Major and trace element results for the studied granitoids

Oxides	NM-04	MS-05	NBG-05B	NBG-06A	NBG-17A	NBG-20A	CHT5	NBG-01A	NBG-02
SiO_2	66.33	67.61	71.24	76.29	73.97	73.31	76.41	69.67	71.70
TiO_2	0.36	0.51	0.33	0.09	0.12	0.11	0.06	0.33	0.22
Al_2O_3	14.95	15.19	13.87	13.52	14.22	14.41	13.61	14.57	13.72
Fe_2O_3	5.35	4.62	3.34	1.00	1.37	1.32	0.73	2.87	3.25
MnO	0.09	0.04	0.08	0.02	0.02	0.02	0.00	0.04	0.03
MgO	1.66	1.24	0.58	0.11	0.02	0.21	0.00	0.83	0.40
CaO	2.27	3.08	1.63	0.73	1.12	1.03	0.41	1.76	1.26
Na_2O	4.41	4.07	4.32	3.16	3.83	3.74	3.02	3.95	3.97
K_2O	3.55	3.13	3.87	5.55	4.96	5.02	5.68	4.42	4.47
P_2O_5	0.12	0.13	0.12	0.03	0.04	0.04	0.00	0.11	0.08
Total	99.10	99.61	99.38	100.50	99.67	99.21	99.92	98.55	99.10
Cs	4.00	1.48	1.41	1.01	2.05	2.07	3.64	2.05	2.45
Rb	95.93	48.05	150.43	172.78	183.31	222.54	151.92	156.43	178.23
Ba	116.21	85.68	525.88	488.04	437.19	563.33	9.89	668.94	544.43
Th	4.43	4.38	12.88	28.38	20.91	21.18	20.11	16.59	39.77
U	1.52	1.66	1.28	2.67	3.59	7.00	5.09	1.64	5.42
Nb	10.99	5.24	2.04	5.90	3.01	7.92	7.56	14.82	10.80
Ta	1.09	0.51	0.18	0.30	0.07	0.32	0.92	0.50	0.50
Pb	9.77	6.10	16.45	20.14	16.83	19.01	42.57	19.28	18.89
Sr	414.31	244.03	276.73	277.02	248.28	283.74	4.78	320.15	276.44
Hf	6.26	6.60	4.79	5.08	7.28	5.81	3.06	10.26	10.31
Zr	324.22	345.27	186.30	185.47	286.18	211.31	75.79	458.29	437.26
Ti	2188	3047	1978	540	719	659	360	1978	1307
Y	11.91	14.22	8.38	21.86	13.29	24.69	9.75	59.89	41.83
Sc	4.84	6.21	3.42	3.80	4.32	4.48		7.37	5.73
V	53.05	36.35	10.68	9.61	8.79	12.43	< L.D.	25.02	15.34
Cr	40.69	20.35	23.38	17.85	32.59	31.49	15.67	26.80	36.07
Co	17.22	11.11	1.92	1.62	1.97	1.81		4.56	2.70
Ni	10.36	6.52	5.84	6.37	6.01	5.96	< L.D.	7.26	6.69
Cu	1.04	2.05	0.91	0.93	0.91	0.93		1.19	0.98
Zn	26.21	48.45	23.54	18.29	23.45	16.59	23.26	49.21	76.53
Ga	19.37	11.24	18.36	17.05	19.00	18.99	16.73	22.17	20.62
La	27.61	22.37	45.69	28.44	50.82	33.02	21.96	87.16	72.61
Ce	51.61	41.99	83.59	53.07	94.95	62.08	47.73	167.27	136.16
Pr	5.92	5.36	10.12	6.82	11.56	7.74	5.16	21.93	17.01
Nd	21.39	22.96	29.15	21.08	33.73	23.51	16.38	69.82	50.82
Sm	4.07	4.83	4.24	3.94	5.18	4.09	2.87	12.46	8.44
Eu	0.99	1.10	0.64	0.70	0.73	0.73	0.21	1.66	1.10
Gd	2.44	3.04	2.52	2.80	3.24	2.92	1.96	8.65	5.81
Tb	0.36	0.44	0.33	0.53	0.46	0.56	0.29	1.59	1.04
Dy	1.83	2.18	1.28	2.63	1.84	2.87	1.61	7.84	5.18
Ho	0.36	0.43	0.24	0.57	0.37	0.63	0.35	1.64	1.10
Er	0.92	1.12	0.60	1.65	1.01	1.85	0.96	4.55	3.09
Tm	0.13	0.16	0.08	0.25	0.15	0.29	0.17	0.67	0.46
Yb	0.84	1.07	0.60	1.76	1.10	2.15	1.16	4.54	3.31
Lu	0.12	0.16	0.11	0.28	0.20	0.36	0.19	0.71	0.54
$(La/Yb)_N$	21.74	13.75	50.39	10.68	30.39	10.14	12.50	12.68	14.48
$(Gd/Yb)_N$	2.34	2.27	3.38	1.28	2.36	1.09	1.36	1.53	1.41
Eu/Eu*	0.97	0.89	0.61	0.65	0.55	0.65	0.28	0.50	0.48
Cr/V	0.77	0.56	2.19	1.96	3.71	2.53		1.07	2.35

NBG-03B	NBG-04A	NBG-14	NBG-18	NBG-19B	NBG-22A	NBG-24B	CHT2	CHT3	CHT4
71.23	72.39	72.86	70.55	69.15	71.45	75.28	73.65	74.42	73.75
0.22	0.19	0.26	0.26	0.55	0.20	0.11	0.21	0.18	0.18
14.02	14.14	13.91	14.35	14.65	14.47	13.98	14.01	13.72	13.97
3.01	2.65	2.46	2.81	4.23	2.64	1.45	1.69	1.59	1.58
0.03	0.03	0.04	0.04	0.04	0.03	0.04	0.03	0.00	0.03
0.49	0.53	0.58	0.56	0.85	0.49	0.14	0.32	0.26	0.32
1.58	1.42	1.64	1.73	1.89	1.37	0.97	1.20	1.25	1.36
4.31	4.02	3.99	4.28	4.40	4.01	2.83	3.91	3.54	3.25
4.11	4.43	3.90	3.96	3.54	4.59	5.31	4.51	4.68	5.21
0.07	0.07	0.08	0.10	0.13	0.07	0.05	0.09	0.07	0.08
99.07	99.87	99.72	98.64	99.43	99.32	100.16	99.62	99.71	99.73
1.50	1.57	7.28	1.44	2.38	2.42	11.94	2.13	1.91	1.95
163.70	170.53	253.79	144.18	163.92	177.21	376.47	138.15	169.92	156.68
688.43	555.33	508.23	620.21	408.19	448.34	372.85	517.34	362.98	267.14
20.95	17.04	22.12	16.89	18.52	9.86	20.82	19.91	23.98	21.11
2.32	1.05	4.13	2.00	1.72	3.02	3.24	3.59	3.79	3.39
8.71	7.94	16.97	14.12	8.67	12.28	14.13	13.70	8.35	12.82
0.28	0.28	0.71	0.45	0.34	0.38	0.89	1.26	1.16	2.12
25.95	15.97	18.21	15.36	17.88	16.11	20.18	38.87	23.75	22.80
369.70	287.87	320.23	432.28	273.29	226.76	177.73	218.88	132.43	95.00
9.62	8.35	9.19	9.16	9.56	8.80	6.99	6.43	5.54	6.01
426.84	372.13	398.35	413.52	395.83	388.54	269.64	207.67	173.59	186.94
1319	1139	1559	1559	3297	1199	659	1259	1079	1079
33.73	26.75	51.34	54.73	34.30	39.56	32.80	25.12	30.36	49.10
5.94	5.14	7.02	6.37	3.93	5.52	7.21			
19.77	15.60	23.75	23.69	12.00	15.13	10.57	19.85	14.31	16.43
35.58	33.12	36.94	27.97	34.45	27.83	16.93	29.26	16.58	17.49
4.41	3.06	4.62	3.42	2.13	3.12	2.74			
7.56	6.62	6.40	6.00	5.97	5.91	6.10	< L.D.	< L.D.	< L.D.
1.42	1.04	1.06	1.04	0.96	1.05	1.02			
61.66	56.82	25.84	25.72	28.88	112.61	36.24	51.67	30.30	40.37
22.40	20.14	21.81	21.89	19.03	18.97	20.80	19.70	18.43	20.20
94.52	75.51	78.60	79.66	52.90	52.07	58.41	70.14	47.82	50.51
173.15	141.59	146.71	157.51	98.47	99.47	103.62	140.88	96.90	103.12
20.89	17.17	18.12	20.74	12.15	12.38	13.41	15.44	10.86	11.72
60.48	49.48	55.69	64.76	35.96	37.76	39.98	53.77	37.67	42.70
8.76	7.07	9.46	11.08	6.23	6.83	6.92	8.36	6.90	8.33
1.20	1.08	1.33	1.67	0.86	0.96	0.81	1.31	0.86	0.91
5.64	4.54	6.45	7.52	4.33	4.94	4.68	5.28	6.04	7.74
0.90	0.73	1.16	1.37	0.81	0.95	0.84	0.75	0.95	1.28
4.11	3.35	5.77	6.72	4.10	4.89	3.86	4.48	5.48	7.47
0.88	0.71	1.25	1.42	0.89	1.04	0.80	0.81	1.10	1.64
2.51	1.98	3.70	4.04	2.58	2.93	2.21	2.29	2.95	4.60
0.38	0.29	0.58	0.61	0.40	0.44	0.32	0.36	0.44	0.72
2.72	2.08	4.14	4.15	2.74	3.04	2.28	2.59	2.97	4.86
0.45	0.33	0.67	0.63	0.42	0.46	0.37	0.39	0.45	0.77
22.93	24.02	12.54	12.68	12.74	11.30	16.94	17.88	10.63	6.86
1.67	1.76	1.25	1.46	1.27	1.31	1.65	1.64	1.63	1.28
0.53	0.59	0.53	0.57	0.51	0.51	0.44	0.61	0.42	0.35
1.80	2.12	1.56	1.18	2.87	1.84	1.70	1.47	1.16	1.06

CHT6	BH50C	BH51B	BH54B	IND 413	BC-01	YD 5	NBG-01B	NBG-01C	NBG-03A
72.60	71.00	67.73	72.48	70.66	72.21	73.74	68.59	67.14	70.62
0.24	0.30	0.69	0.30	0.42	0.40	0.32	0.49	0.54	0.27
14.55	14.70	14.74	14.27	14.01	14.51	14.05	14.69	15.38	14.44
1.81	2.74	4.55	2.10	3.68	2.47	2.71	4.23	4.20	2.50
0.00	0.04	0.06	0.00	0.04	0.04	0.08	0.07	0.06	0.04
0.43	0.38	1.24	0.56	0.64	0.42	0.30	1.23	1.25	0.56
1.48	1.83	2.68	1.74	2.07	1.55	1.22	2.50	2.56	1.45
3.72	3.92	3.83	3.91	3.45	3.27	2.55	4.34	4.41	4.06
4.56	4.31	3.27	3.90	4.32	4.83	4.73	2.87	2.72	4.41
0.10	0.09	0.15	0.09	0.13	0.02	0.10	0.16	0.19	0.10
99.49	99.31	98.94	99.35	99.42	99.73	99.80	99.17	98.45	98.45
3.37	1.10	1.14	1.26	1.86	1.81	1.38	2.32	2.43	2.21
163.21	131.68	100.65	118.50	140.39	129.25	104.00	131.17	164.07	221.24
452.97	622.42	433.05	575.41	429.66	316.98	273.65	347.16	582.03	717.27
18.83	18.58	13.70	16.45	22.21	15.99	24.00	19.66	20.14	28.81
1.63	4.46	1.79	0.85	2.05	1.31	2.60	2.15	2.55	2.68
9.67	10.37	21.30	7.37	15.58	15.89	11.19	22.14	22.21	18.76
0.89	0.92	2.02	0.52	0.88	1.30	0.84	0.75	1.21	0.69
25.26	21.03	16.33	18.16	22.98	18.01	29.32	13.87	15.03	22.95
137.35	195.31	253.67	236.18	158.98	198.15	145.66	324.46	404.18	452.63
5.97	6.32	9.29	6.54	10.29	8.21	10.96	11.84	12.36	10.98
209.90	253.75	356.12	246.61	372.63	385.92	463.76	565.10	579.49	476.75
1439	1799	4137	1799	2518	2401	1924	2938	3237	1619
19.92	18.51	54.40	19.24	36.28	35.57	22.41	76.43	117.03	73.73
					4.00	2.88	23.11	9.59	8.21
20.82	27.64	68.16	23.38	38.89	35.38	16.74	46.08	37.24	26.52
16.34	15.93	28.71	16.71	23.95	13.32	13.89	39.47	33.39	37.04
					4.79	20.39	7.90	5.78	4.46
< L.D.	5.38	10.11	6.92	< L.D.	4.64	5.18	7.63	7.04	7.00
					1.59	1.18	1.60	1.31	1.25
44.07	44.78	78.87	44.37	64.83	19.73	26.49	55.02	47.33	32.44
18.32	20.65	21.22	18.91	18.72	21.01	18.62	24.49	25.73	28.11
70.81	93.86	71.74	74.94	93.20	75.87	87.15	91.02	127.75	135.80
140.08	173.16	150.08	141.57	176.98	141.93	150.73	182.53	252.01	252.13
15.25	16.98	17.31	14.24	19.12	15.61	15.83	24.50	33.94	31.05
51.92	55.68	62.42	48.24	64.66	52.21	47.79	78.36	111.28	92.74
7.71	7.24	11.50	8.04	10.42	8.85	7.56	14.11	21.40	15.09
0.95	1.15	2.04	1.10	1.54	1.18	1.02	2.03	2.61	1.99
5.14	6.00	9.84	5.10	8.23	5.54	4.21	9.79	15.24	10.36
0.80	0.72	1.46	0.77	1.29	0.88	0.61	1.82	2.96	1.84
4.08	3.59	9.68	4.20	7.28	5.06	3.04	9.14	15.14	9.12
0.75	0.70	1.91	0.72	1.33	1.08	0.63	1.97	3.15	1.93
2.08	1.84	5.52	2.00	3.79	3.02	1.76	5.68	8.70	5.47
0.31	0.28	0.92	0.25	0.53	0.45	0.26	0.87	1.28	0.82
2.09	1.82	6.61	1.84	3.58	3.16	1.81	6.22	8.40	5.55
0.32	0.30	0.94	0.28	0.53	0.47	0.27	1.01	1.21	0.84
22.41	34.02	7.17	26.85	17.21	15.83	31.82	9.66	10.05	16.15
1.98	2.64	1.20	2.22	1.85	1.41	1.87	1.26	1.46	1.50
0.47	0.54	0.60	0.53	0.52	0.52	0.56	0.53	0.45	0.49
0.78	0.58	0.42	0.71	0.62	0.38	0.83	0.86	0.90	1.40

NBG-4B	NBG-05A	NBG-05C	NBG-05E	NBG-06B	NBG-06C	NBG-07	NBG-08B	NBG-17B
65.96	72.70	66.93	73.86	70.47	69.09	69.44	74.87	67.37
0.73	0.14	0.66	0.13	0.32	0.56	0.53	0.13	0.64
15.25	14.39	15.28	14.13	14.64	14.28	14.67	13.97	14.97
5.46	2.24	5.03	2.07	3.46	3.93	3.58	1.50	4.63
0.08	0.03	0.08	0.03	0.04	0.06	0.07	0.02	0.06
1.44	0.31	2.04	0.08	0.58	2.04	0.68	0.09	1.03
2.88	1.26	3.01	1.11	1.62	2.33	2.07	1.13	2.45
4.89	4.01	4.52	3.47	4.32	4.52	4.19	3.12	4.55
1.83	4.30	2.96	5.51	4.46	2.46	3.11	5.21	3.32
0.23	0.04	0.38	0.05	0.12	0.38	0.14	0.03	0.17
98.75	99.42	100.89	100.44	100.03	99.65	98.48	100.07	99.19
3.30	2.06	2.01		2.08	2.88	3.53		3.82
180.71	139.57	134.78		179.33	157.43	200.28		136.43
418.22	475.12	236.79		637.49	295.00	467.93		205.65
31.00	22.98	15.81		23.92	33.34	18.79		21.45
2.40	1.88	2.76		1.79	3.47	4.08		4.75
13.34	9.76	11.82		17.56	13.95	19.16		15.04
0.37	0.44	0.69		0.74	0.61	0.63		0.39
18.27	15.04	12.18		18.34	16.16	18.29		15.63
252.61	304.34	515.33		364.50	310.35	326.15		267.59
14.08	9.34	12.85		9.77	14.00	14.72		14.51
636.90	429.27	609.81		435.05	663.67	729.55		714.05
4376	839	3957		1918	3357	3177		3843
49.86	32.55	319.51		68.92	47.06	71.07		55.05
5.31	5.96	28.45		6.64	8.82	9.25		10.47
15.85	19.01	61.36		23.18	20.27	36.28		27.04
36.26	23.30	35.70		29.34	31.62	35.18		28.87
3.68	3.52	10.44		3.72	4.71	6.12		5.34
6.47	6.23	8.04		6.24	6.46	6.99		6.71
1.31	1.06	1.29		1.08	1.05	1.34		1.20
30.99	25.15	52.01		73.19	79.81	43.45		32.47
25.83	23.06	26.50		23.59	25.61	23.93		25.98
146.31	115.11	82.56		116.97	140.63	107.59		106.86
284.93	208.12	184.04		219.57	253.18	211.41		206.36
36.69	24.58	28.41		27.40	29.43	27.53		26.58
113.19	69.31	102.38		83.64	82.46	87.28		82.41
19.14	9.61	23.44		14.24	11.40	15.18		14.11
1.72	1.28	3.05		1.88	1.44	1.97		1.54
11.65	6.10	19.54		9.95	7.53	10.52		9.42
1.74	0.91	4.86		1.77	1.17	1.85		1.60
7.04	4.16	21.03		8.83	5.54	8.86		7.29
1.39	0.88	4.02		1.84	1.20	1.87		1.48
3.71	2.44	11.19		5.09	3.50	5.34		4.00
0.52	0.36	1.53		0.75	0.54	0.81		0.58
3.58	2.57	9.64		4.89	3.87	6.20		4.03
0.57	0.42	1.49		0.74	0.63	1.12		0.66
27.01	29.53	5.66		15.80	24.02	11.46		17.52
2.62	1.90	1.63		1.63	1.56	1.36		1.88
0.36	0.52	0.44		0.49	0.48	0.48		0.41
2.29	1.23	0.58		1.27	1.56	0.97		1.07

NBG-19A	NBG-20B	NBG-20C	NBG-22B	BH51C	AC-01	BH50A	BH50B	BH51A	BH52
75.08	70.83	70.26	66.77	69.87	63.69	73.49	70.01	72.29	73.52
0.14	0.38	0.36	0.58	0.46	0.62	0.16	0.51	0.27	0.27
13.75	14.56	14.77	14.85	14.18	15.70	14.10	14.43	13.73	13.77
1.22	3.10	3.19	5.36	3.47	5.85	1.17	3.26	2.03	1.90
0.02	0.06	0.06	0.09	0.06	0.07	0.02	0.05	0.03	0.04
0.16	0.81	0.67	1.17	0.75	2.63	0.31	0.76	0.34	0.40
1.20	1.99	1.97	2.54	2.29	3.40	1.66	2.14	1.69	1.26
2.91	4.56	4.56	4.16	4.16	3.62	3.35	3.90	3.75	3.91
5.63	3.15	3.58	2.90	3.08	4.04	4.61	3.61	4.43	4.38
0.05	0.13	0.14	0.17	0.15	0.09	0.05	0.16	0.08	0.07
100.16	99.57	99.56	98.59	98.47	99.71	98.92	98.83	98.64	99.52
4.13	4.68	4.00	2.07	1.40	2.09				
181.55	195.07	199.83	155.34	117.17	137.73	116.00	133.00	119.00	133.00
83.83	393.29	558.52	640.97	287.97	176.74	338.00	533.00	548.00	571.00
33.28	25.05	24.01	16.78	24.38	16.93	10.00	14.00	14.00	17.00
2.38	4.26	4.85	2.41	1.71	3.07				
31.73	26.61	29.54	22.55	21.45	77.76	6.00	20.00	12.00	17.00
0.91	0.98	1.64	0.73	2.40	9.97				
12.80	19.06	17.62	12.95	19.73	13.54	19.00	16.00	19.00	34.00
276.23	288.52	393.51	400.74	155.22	401.91	235.00	246.00	200.00	232.00
19.95	15.09	11.77	14.12	9.93	17.14				
1004.10	721.71	516.63	700.00	392.14	815.53	117.00	311.00	202.00	211.00
839	2278	2158	3477	2758	3714	959	3057	1619	1619
176.29	105.47	79.55	93.22	63.24	243.71	13.00	58.00	28.00	27.00
14.33	10.54	10.25	10.77		19.81				
45.69	29.27	34.45	38.66	37.56	159.88	14.00	50.00	33.00	23.00
15.65	40.35	37.42	29.76	41.09	60.07	15.00	27.00	22.00	23.00
8.35	5.14	4.78	6.35		28.00				
7.27	7.02	6.18	6.68	8.93	13.16	1.00	5.00	5.00	5.00
1.40	1.07	1.16	1.28		2.87				
30.52	57.12	49.12	33.89	69.83	63.83	27.00	66.00	38.00	53.00
32.50	25.95	26.10	25.71	22.73	29.50	16.00	19.00	17.00	17.00
169.82	108.49	100.37	111.26	95.57	95.11				
338.77	210.82	195.24	217.22	195.99	213.23				
45.10	27.82	25.17	28.35	21.38	26.76				
149.75	89.50	78.83	91.98	75.64	111.95				
33.03	17.24	14.05	16.94	13.59	24.50				
2.74	1.84	2.02	2.28	1.76	3.27				
24.13	12.57	9.52	12.39	11.27	18.62				
4.93	2.49	1.79	2.35	1.86	3.56				
24.82	12.87	9.07	11.71	10.89	25.09				
4.98	2.75	2.00	2.48	2.26	6.06				
13.14	7.87	5.96	6.98	6.34	19.18				
1.83	1.20	0.94	1.04	0.99	3.19				
11.57	8.30	6.97	7.05	6.49	22.88				
1.80	1.28	1.13	1.09	0.93	3.37				
9.70	8.63	9.51	10.43	9.73	2.74				
1.68	1.22	1.10	1.41	1.40	0.65				
0.30	0.39	0.54	0.49	0.44	0.47				
1.22	1.38	1.09	0.77	1.09	0.38	1.07	0.54	0.67	1.00

MJ-1	MJ-2	MJ-3	MJ-4a	MJ-5	MJ-6	MJ-7	MJ-8	MJ-9a	MJ-10	MJ-11	PAN-01	PAN-02
68.38	63.89	69.10	69.02	73.06	73.43	70.16	71.57	69.75	70.76	71.72	68.92	66.57
0.63	0.76	0.51	0.52	0.30	0.17	0.44	0.29	0.54	0.35	0.33	0.54	0.48
14.99	15.38	14.14	14.37	13.61	14.30	14.01	14.31	14.46	14.12	13.90	15.19	15.15
4.62	6.04	3.96	3.34	2.79	1.69	3.62	2.95	4.04	3.16	2.94	4.14	4.90
0.08	0.10	0.08	0.09	0.03	0.02	0.05	0.03	0.09	0.05	0.04	0.07	0.01
1.11	1.96	1.05	1.10	0.45	0.33	0.69	0.58	1.01	0.71	0.44	0.90	1.29
2.69	3.25	2.46	2.59	1.67	1.51	2.20	1.90	2.36	2.06	1.75	1.40	2.58
4.14	4.50	4.44	4.76	3.62	3.96	4.01	3.99	4.30	4.30	4.14	3.12	3.84
3.75	1.39	3.37	2.78	4.14	3.89	3.61	3.79	2.61	3.41	3.82	4.75	4.23
0.13	0.27	0.13	0.15	0.06	0.03	0.09	0.09	0.11	0.08	0.07	0.12	0.11
100.50	97.54	99.23	98.72	99.73	99.33	98.88	99.50	99.27	99.00	99.14	99.15	99.16
											2.60	3.82
											213.16	183.97
											483.31	518.08
											33.68	15.12
											5.40	4.33
											38.10	42.64
											1.84	2.52
											29.06	18.12
											126.89	134.57
											30.84	28.64
											1340.77	1263.67
3765	4556	3027	3141	1799	1001	2638	1739	3225	2098	1966	3225	2848
											119.78	118.36
											10.04	11.64
											42.85	51.62
											20.32	24.57
											15.67	17.07
											5.68	7.18
											1.78	1.79
											36.54	24.81
											25.19	22.08
											146.63	83.42
											293.09	185.65
											34.01	23.49
											125.72	99.46
											24.63	22.72
											2.67	2.92
											17.04	16.36
											2.78	2.74
											16.57	16.77
											3.45	3.51
											9.62	9.56
											1.43	1.38
											9.79	9.37
											1.44	1.38
											9.89	5.88
											1.40	1.40
											0.40	0.47
0.45	0.35	0.43	0.37	0.56	1.06	0.48	0.89	0.24	0.53	0.61	0.47	0.48

Table 5: Results for whole-rock Sm-Nd isotope measurements by TIMS

Sample	Age (Ma)	Sm (ppm)	Nd (ppm)	147Sm/ 144Nd	2σ	143Nd/ 144Nd	2σ	143Nd/ 144Nd (t)	2σ	εNd (3.0 Ga)	2σ
Bellur-Nagamangala											
BH50c	3000	7.55	55.0	0.0830	0.0003	0.510354	0.000008	0.508709	0.000010	-0.7	0.2
BH51c	3000	13.3	74.9	0.1076	0.0004	0.510856	0.000008	0.508724	0.000010	-0.4	0.2
BH 51b	3000	11.5	63.8	0.1087	0.0004	0.510865	0.000003	0.508711	0.000004	-0.7	0.1
CHT2	3000	8.08	50.0	0.0978	0.0004	0.510633	0.000004	0.508696	0.000005	-1.0	0.1
CHT3	3000	6.55	36.3	0.1091	0.0004	0.510863	0.000003	0.508701	0.000004	-0.9	0.1
CHT4	3000	7.86	39.2	0.1211	0.0005	0.511081	0.000002	0.508682	0.000002	-1.3	0.05
CHT6	3000	9.89	42.3	0.1413	0.0006	0.511510	0.000004	0.508710	0.000005	-0.7	0.1
Ind 413	3000	10.7	66.2	0.0976	0.0004	0.510708	0.000004	0.508774	0.000005	0.5	0.1
CHT5	3000	2.8	15.8	0.1066	0.0004	0.510771	0.000003	0.508659	0.000004	-1.7	0.1
W of Bellur											
BH54b	3000	7.47	47.4	0.0953	0.0004	0.510610	0.000004	0.508722	0.000005	-0.5	0.1

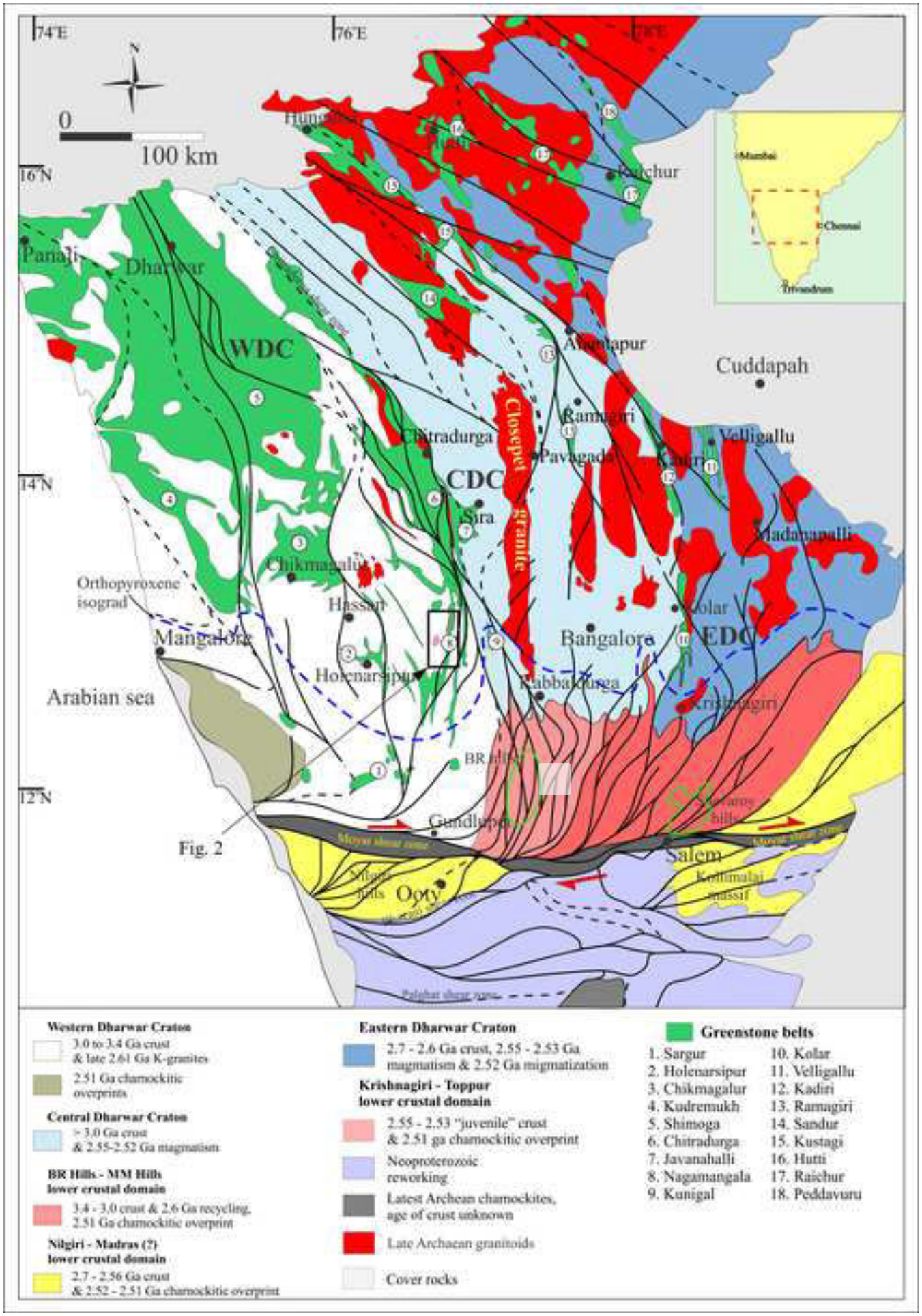

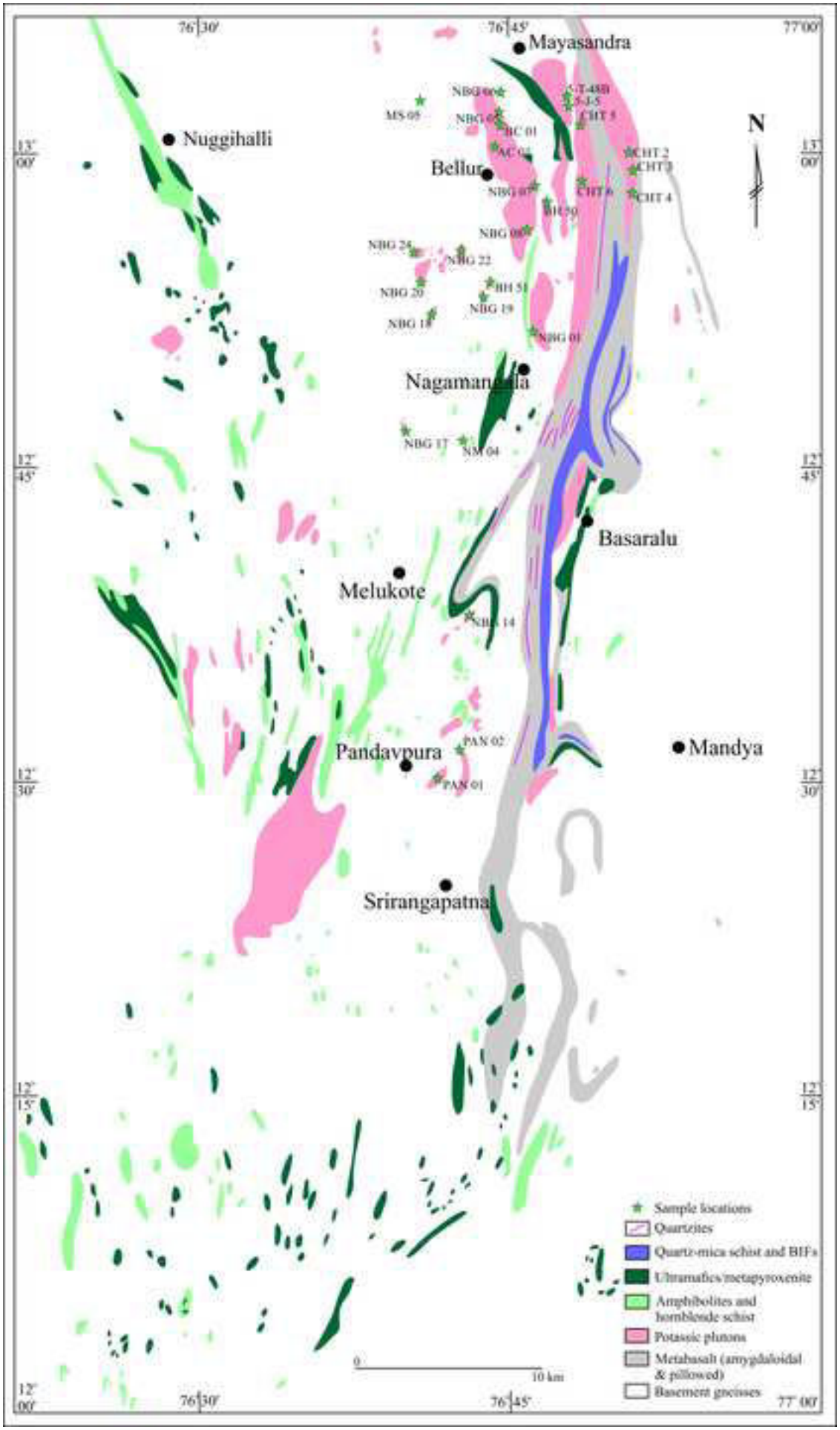

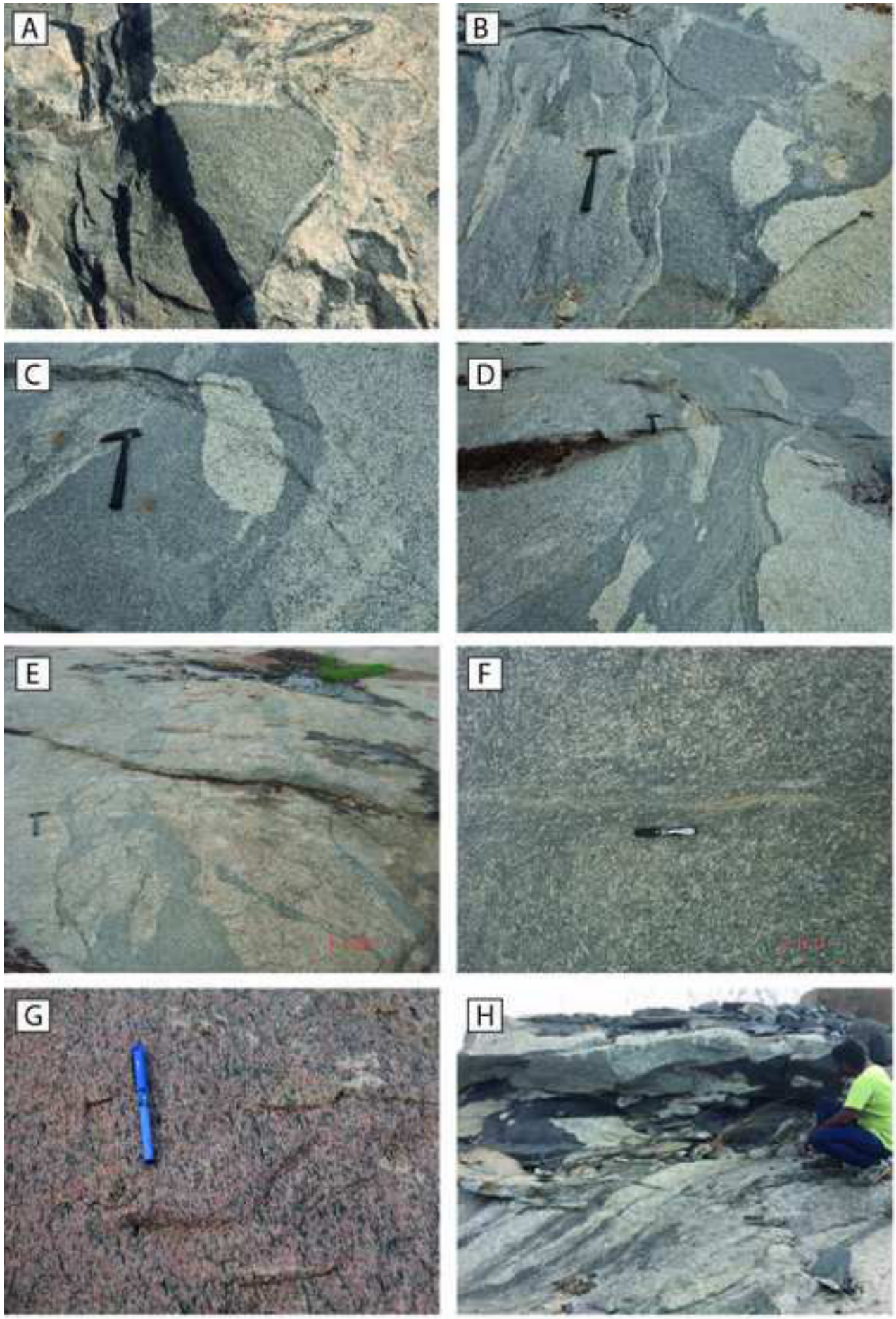

Figure 3

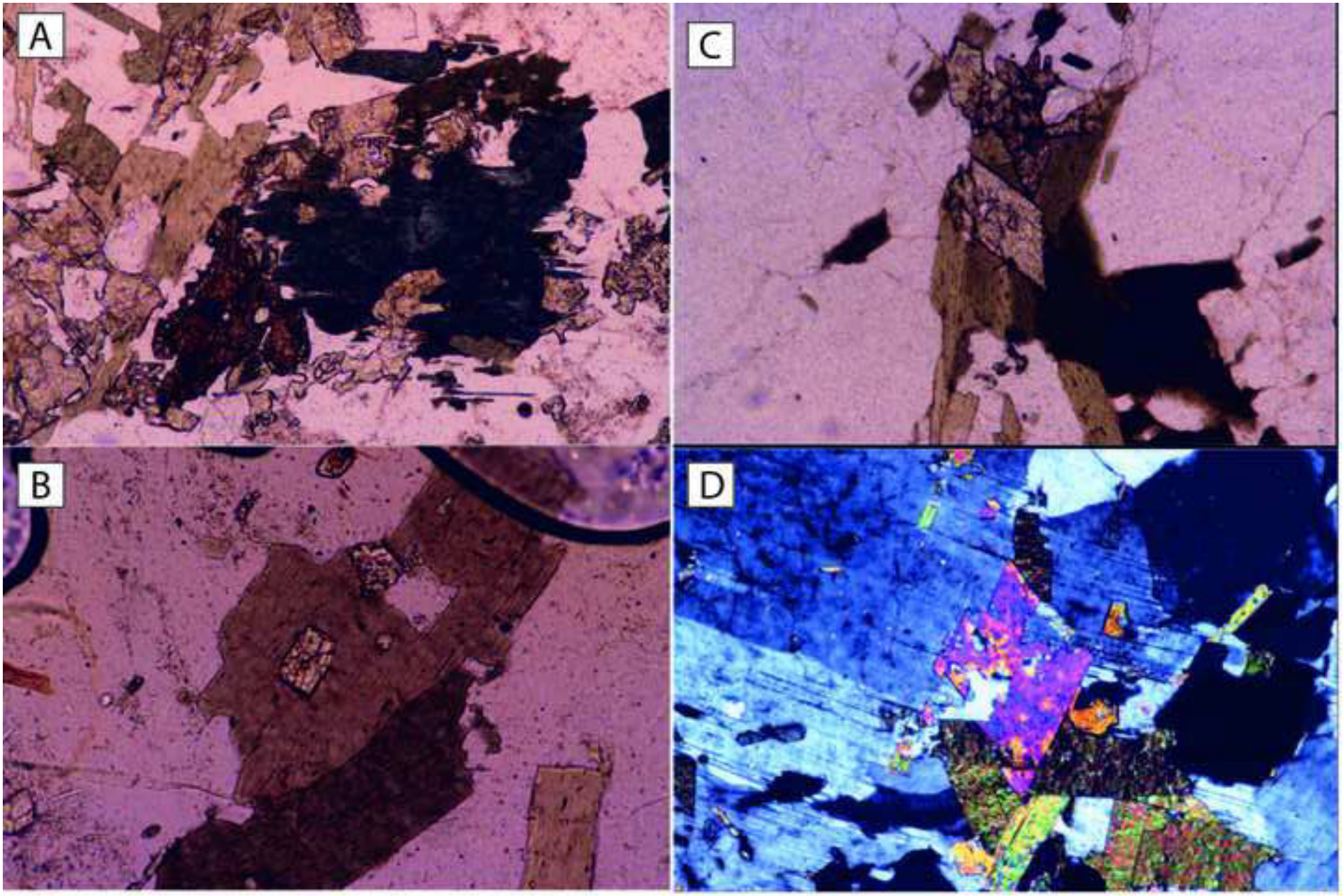

Figure 4

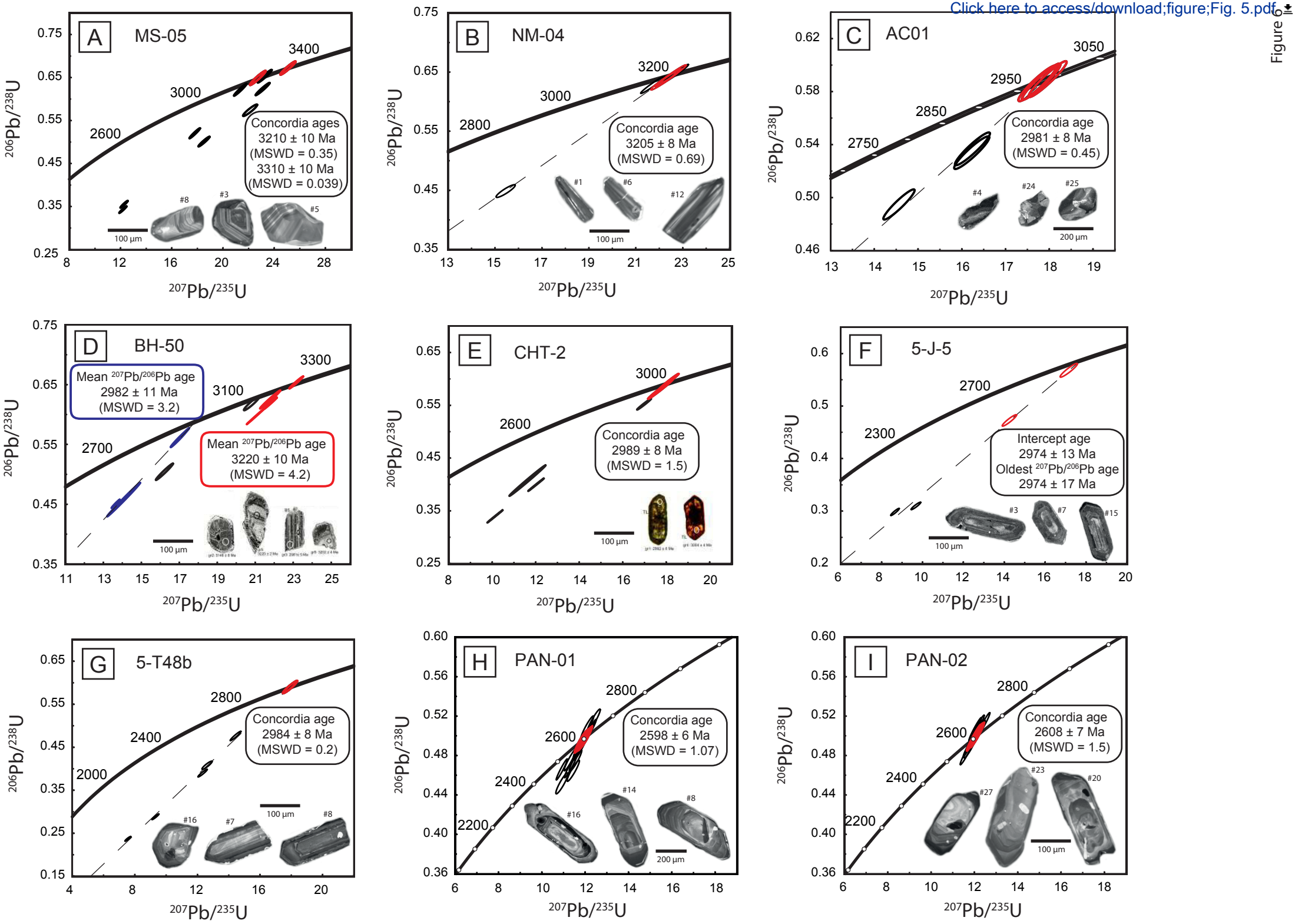

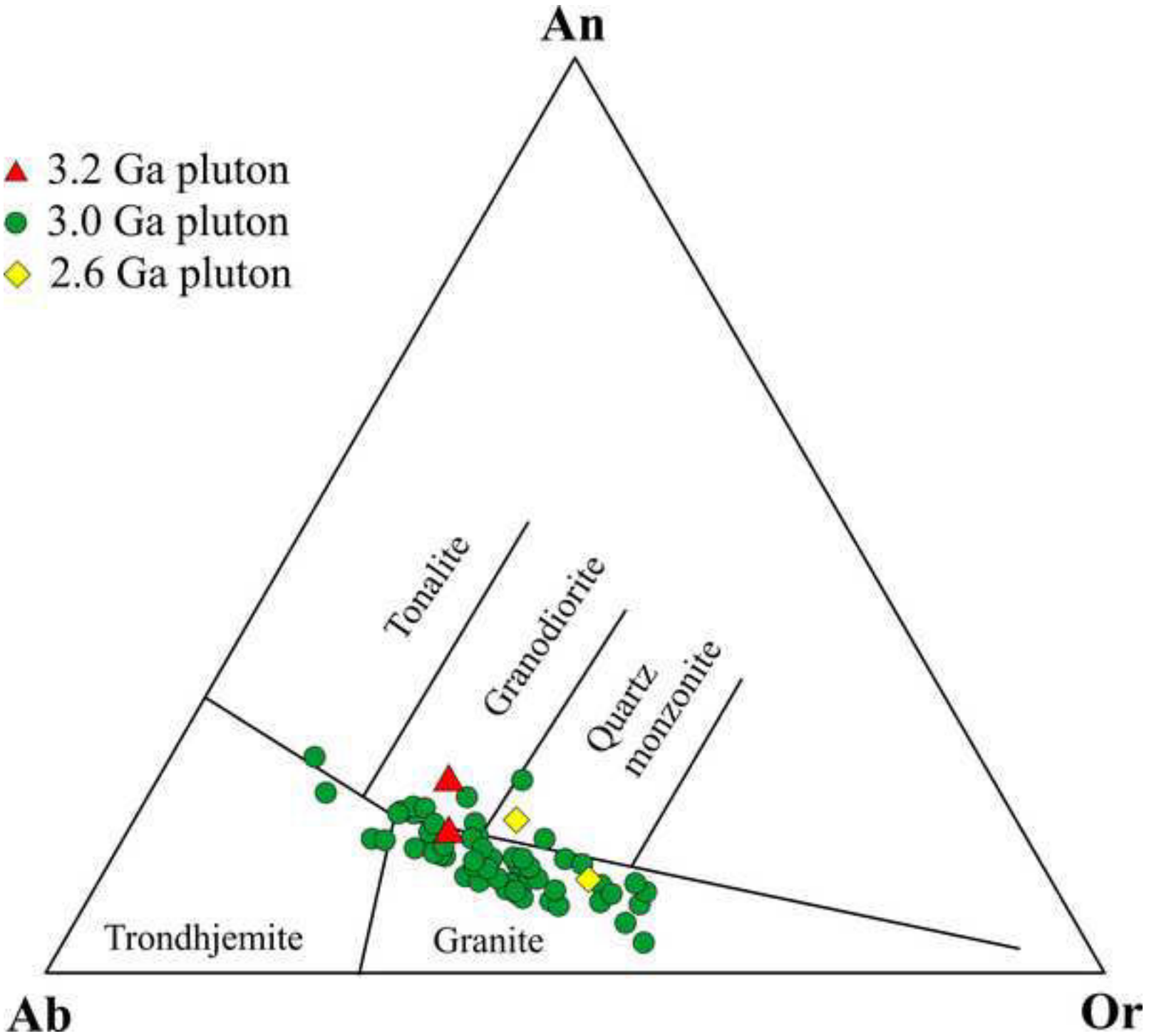

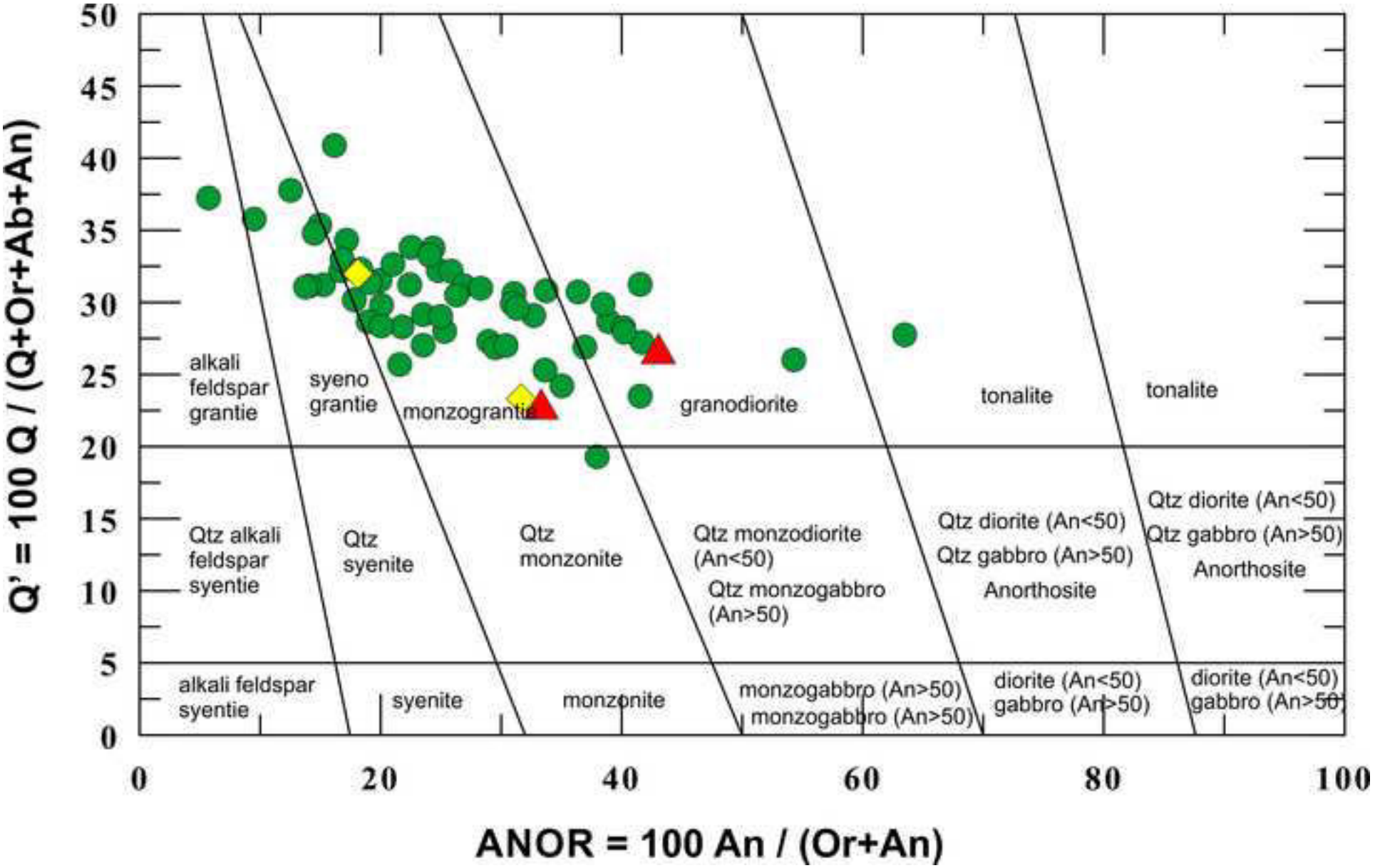

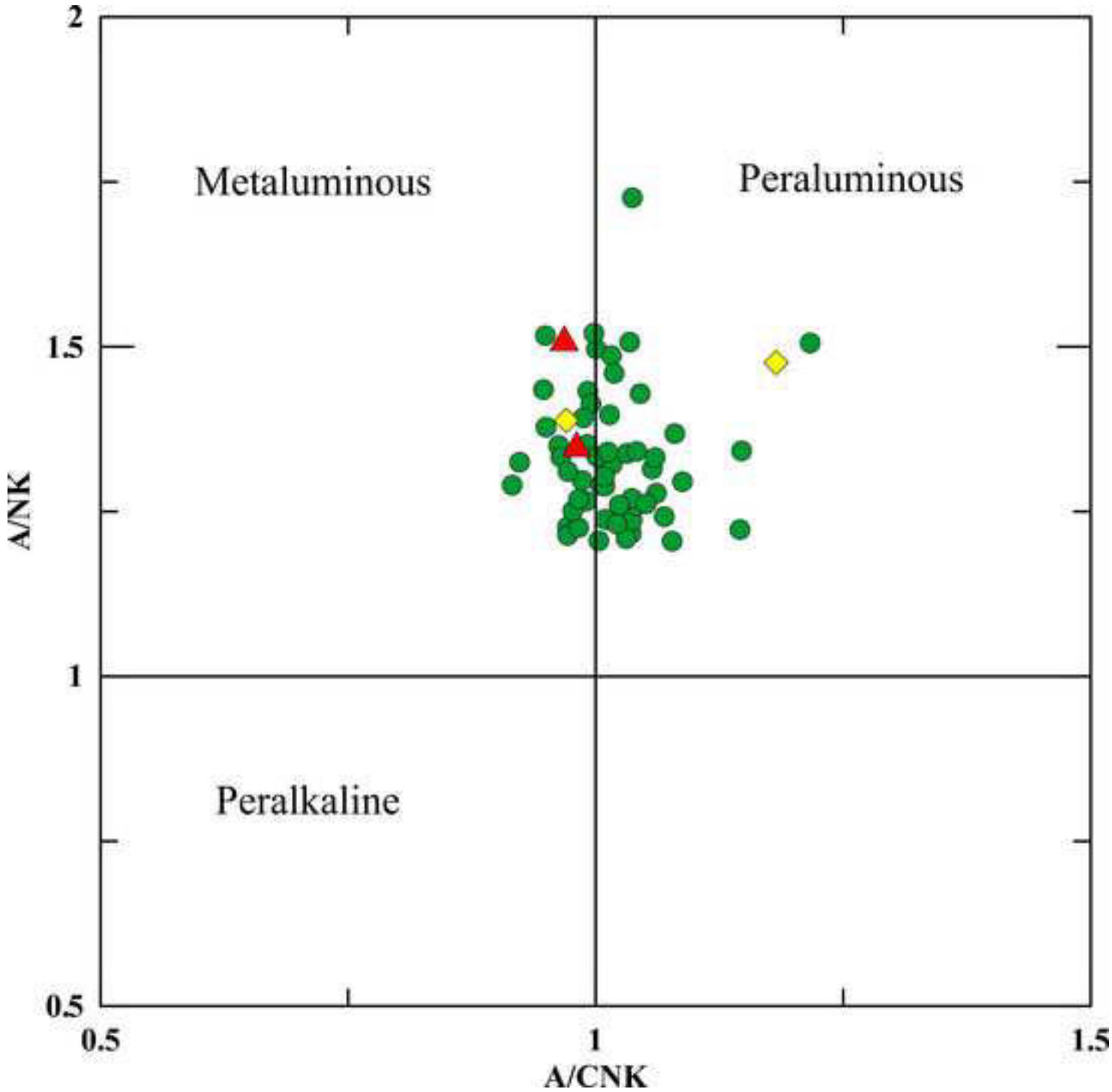

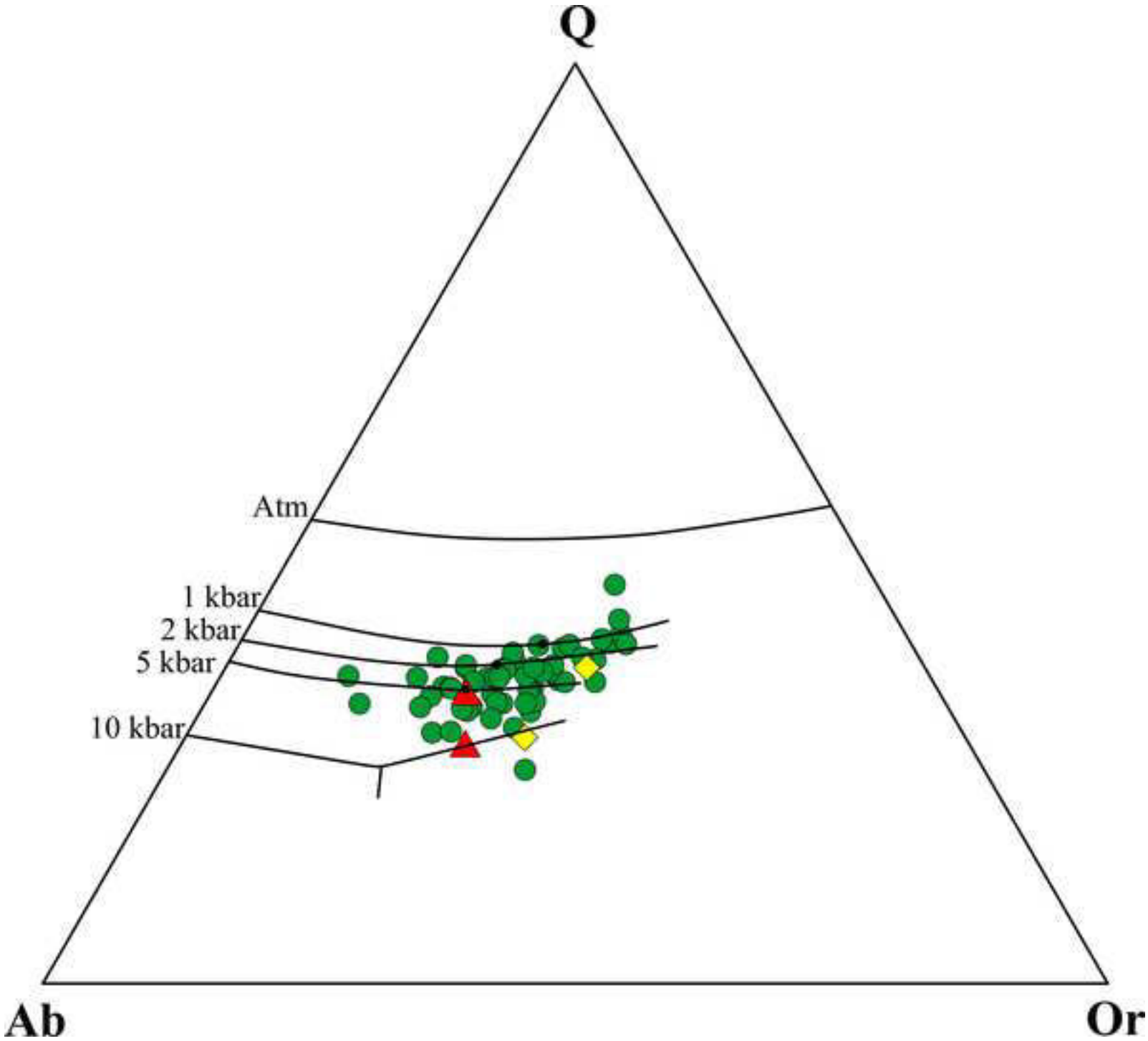

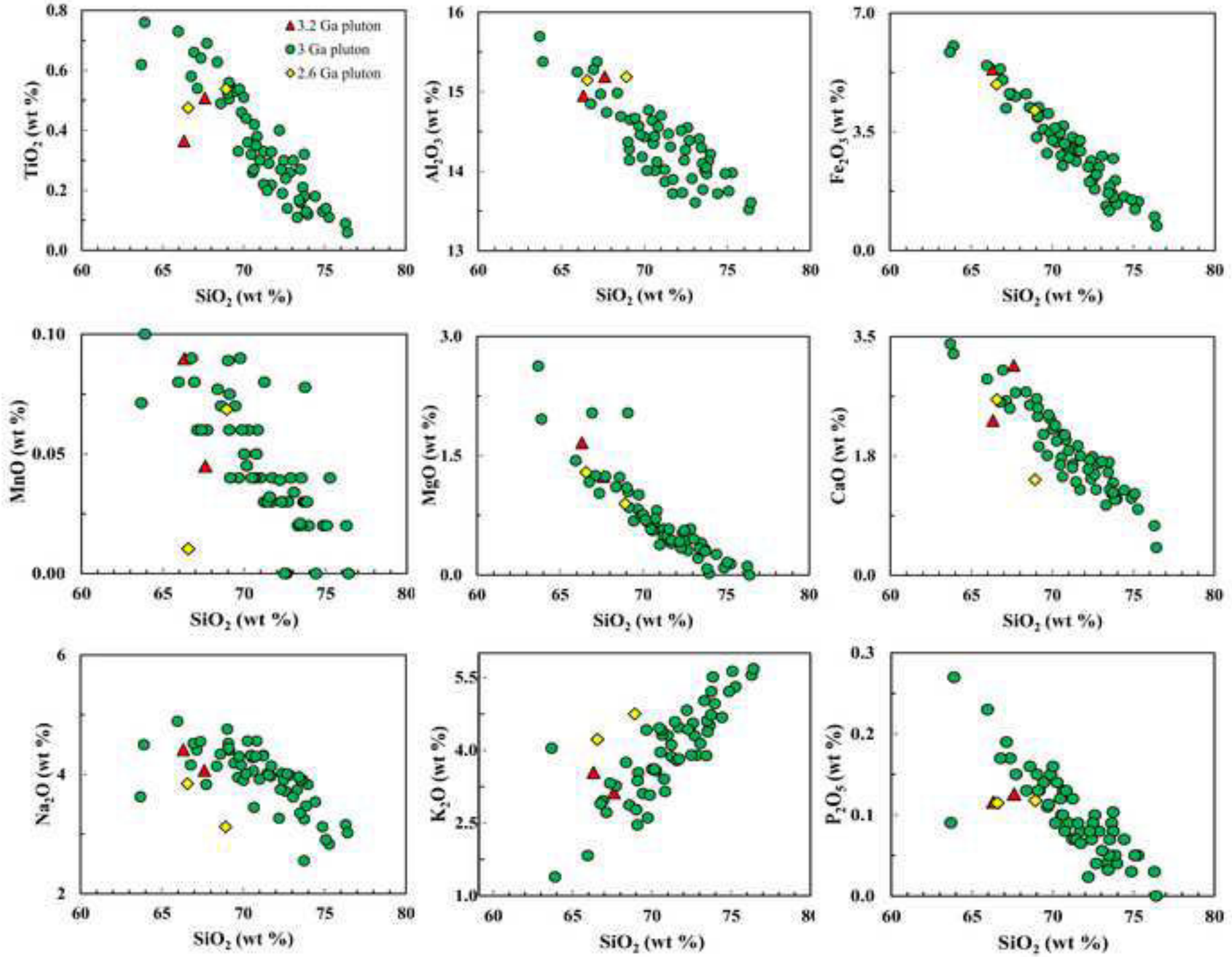

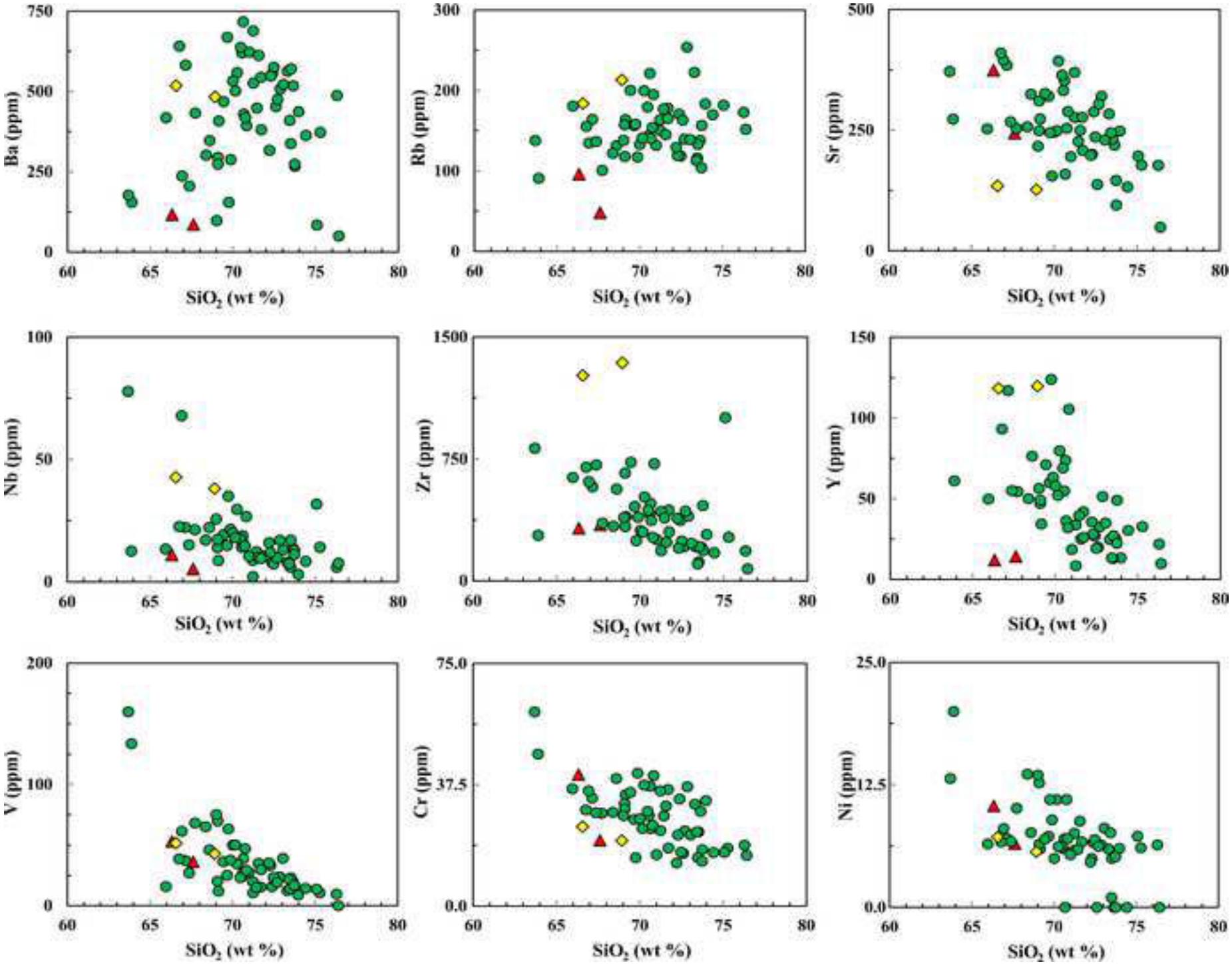

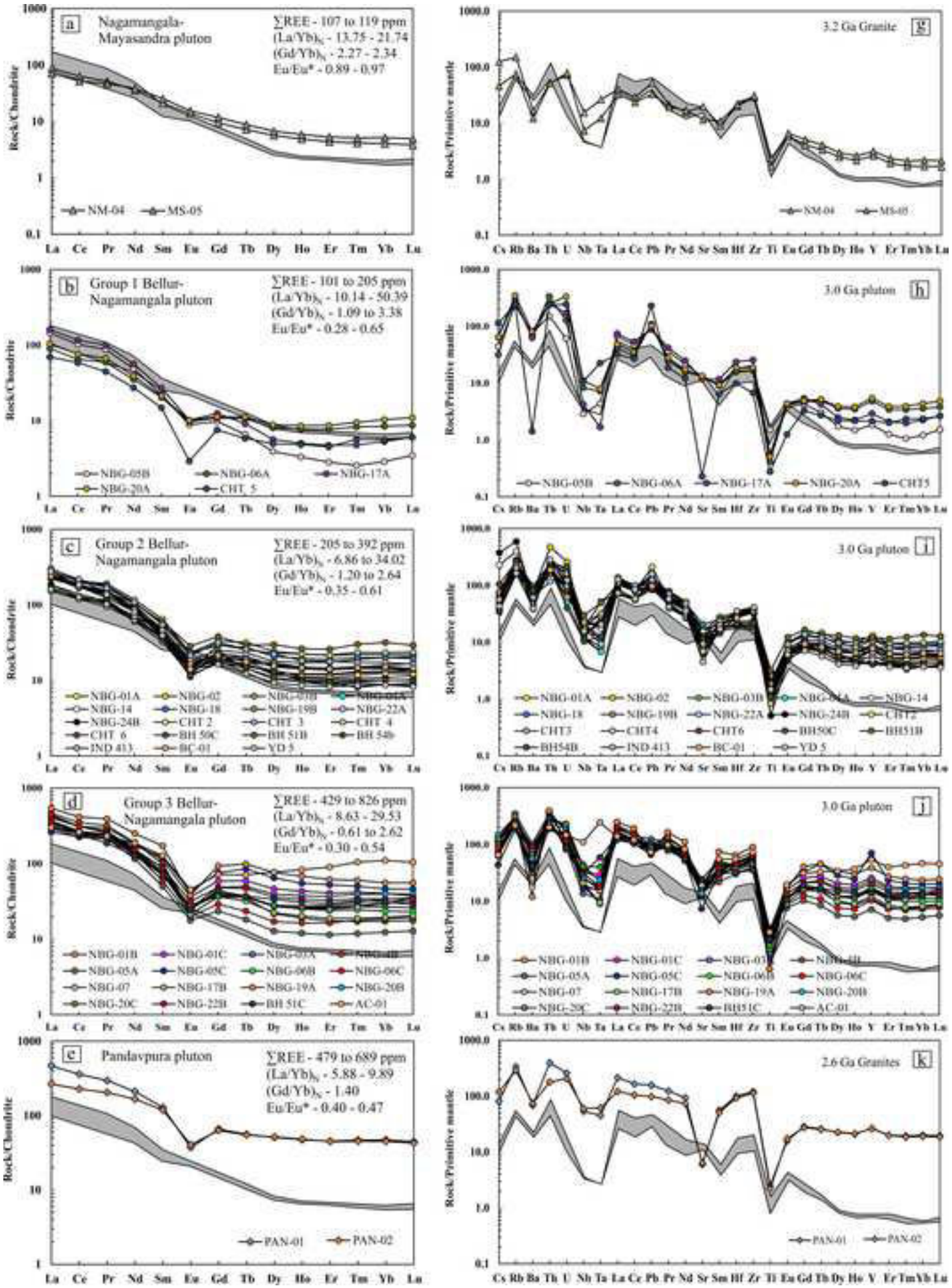

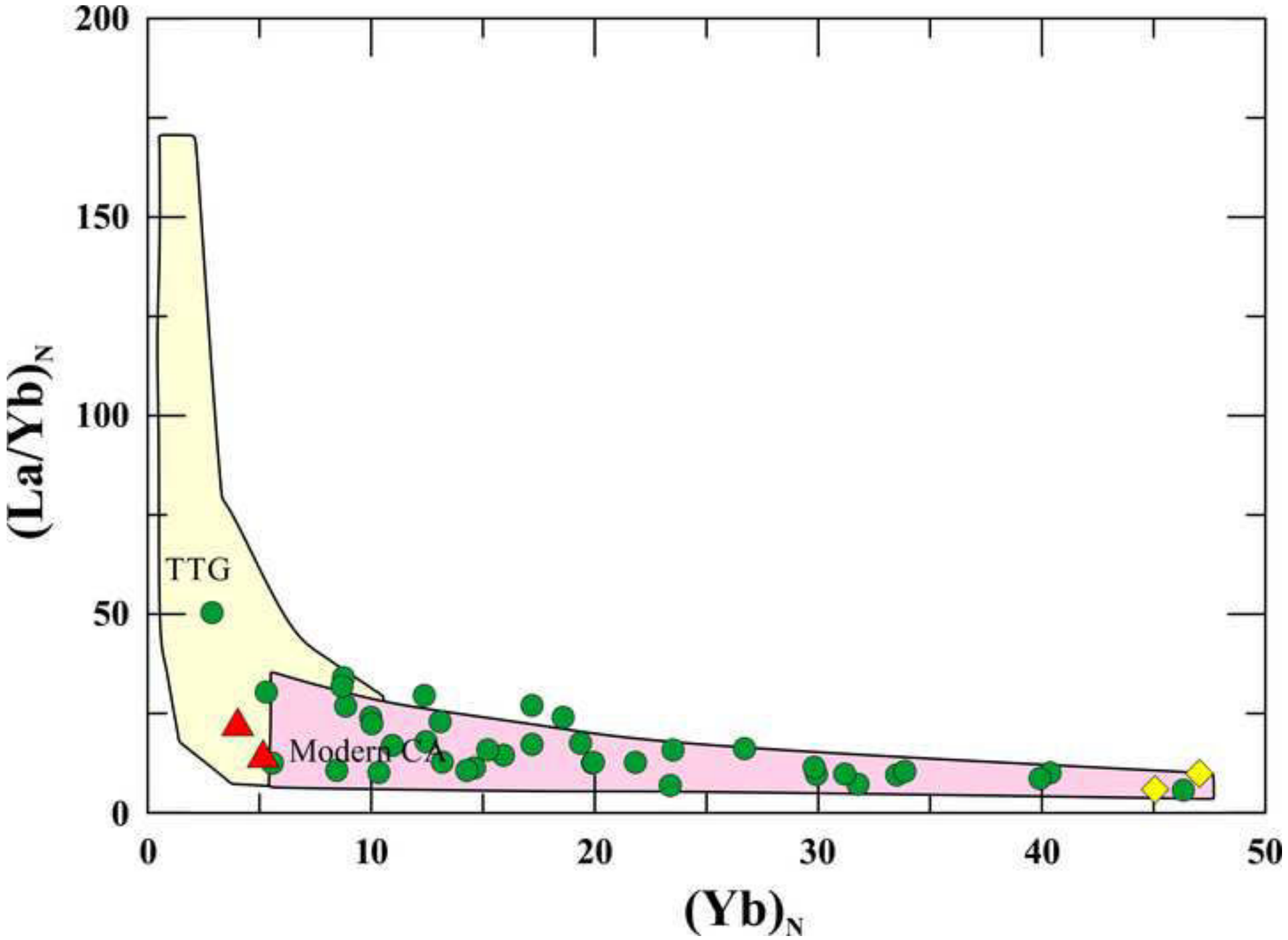

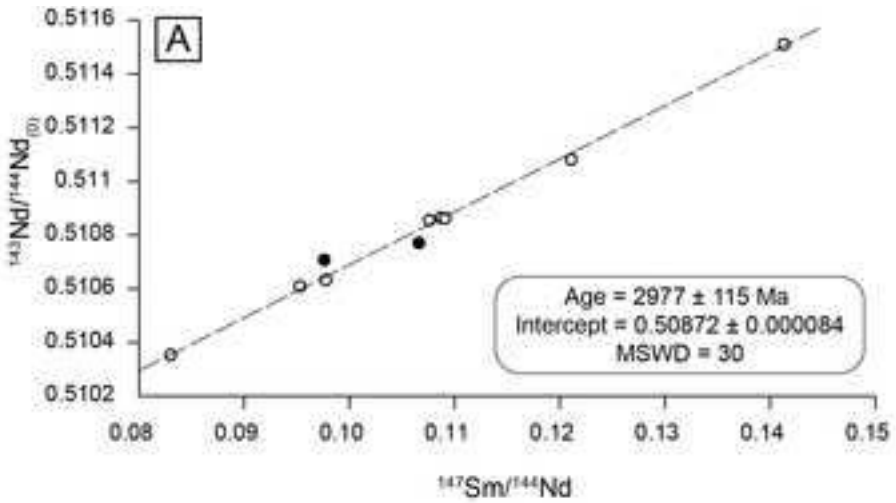

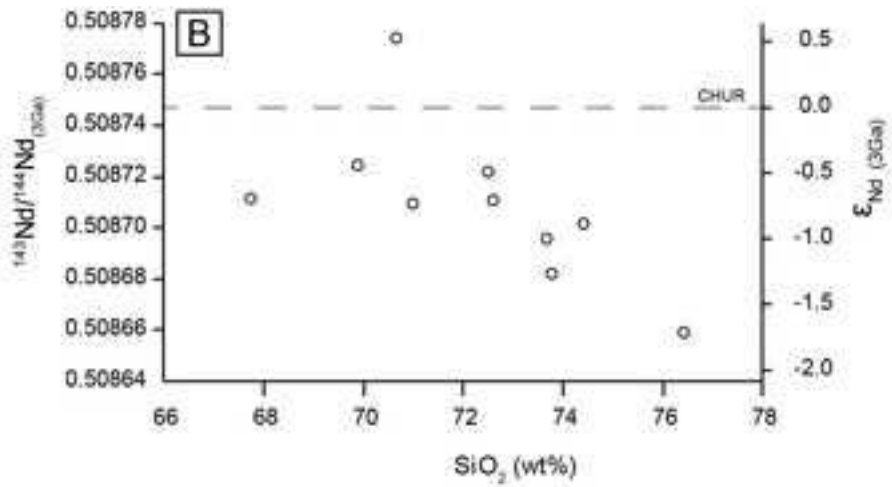

Figure 13